Supporting information for

Crystalline Pseudorotaxane Enabling Dual-Wavelength Photothermal Mechanical Actuation

Kuan-Hung Huang,[a] Hong-Kai Chang,[a] Meng-Che Tsai,[a,c] Ting-Wei Liao,[a,c] You-Ting Chen,[a] Chu-Liang Hsieh,[a,c] Pei-Lin Chen,[b] Kai-Jen Chen,*[a,c] and Masaki Horie*[a,c]

[a] *Department of Chemical Engineering, National Tsing Hua University, 101, Section 2, Kuang-Fu Road, Hsinchu 30013, Taiwan.*

[b] *Instrumentation Center, National Tsing Hua University, 101, Section 2, Kuang-Fu Road, Hsinchu 30013, Taiwan.*

[b] *Research Institute for Electronic Science (RIES), Hokkaido University, N21W10, Kita-Ward, Sapporo 001-0021, Japan.*

Correspondence Address

Research Institute for Electronic Science (RIES), Hokkaido University, N21W10, Kita-Ward, Sapporo 001-0021, Japan.

Email: kjchen@es.hokudai.ac.jp and mhorie@es.hokudai.ac.jp

Table of contents

S1. ^{1}H NMR and Mass Spectra

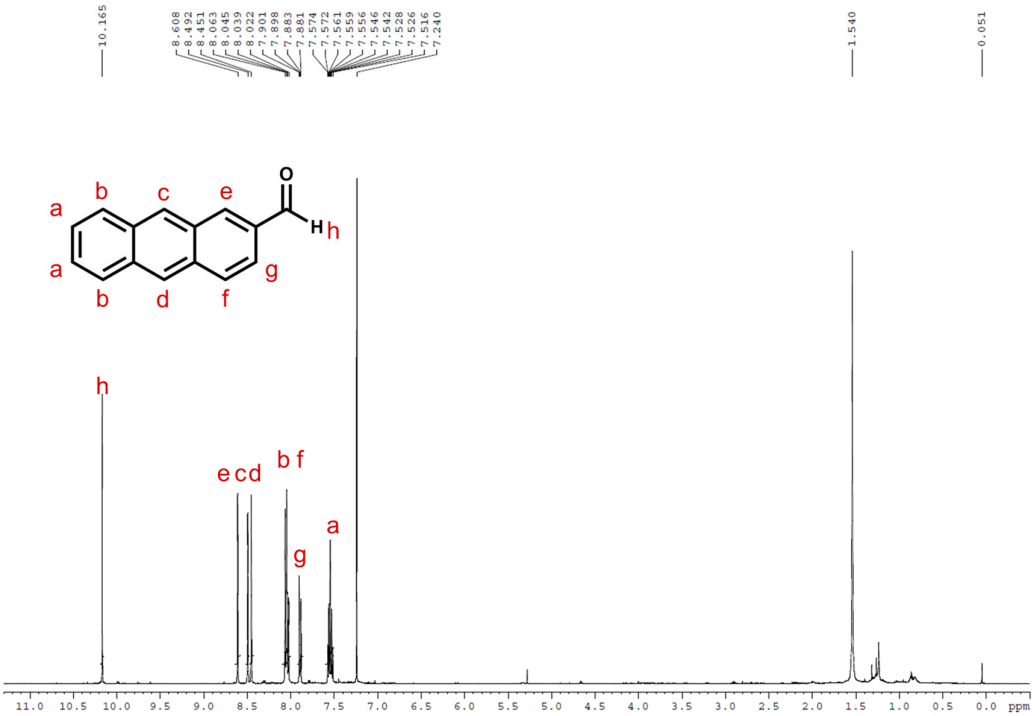

Fig. S1. ^{1}H NMR spectrum (500 MHz, $CDCl_3$, 24.9 °C (298 K)) of anthracene-2-carbaldehyde

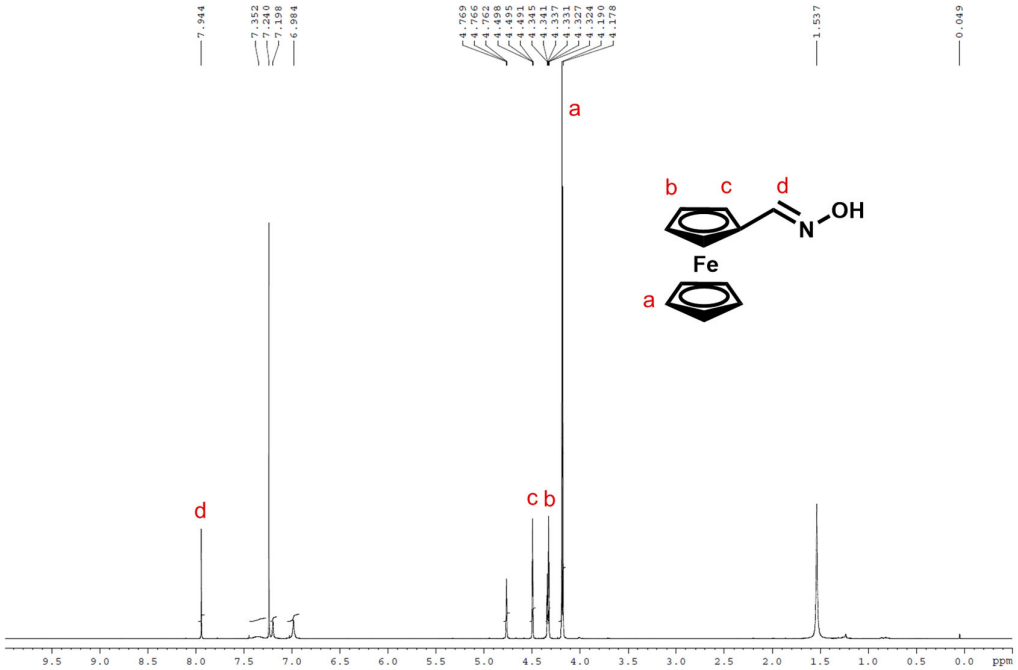

Fig. S2. ^{1}H NMR spectrum (500 MHz, $CDCl_3$, 24.9 °C (298 K)) of ferrocenecarbaldehyde oxime

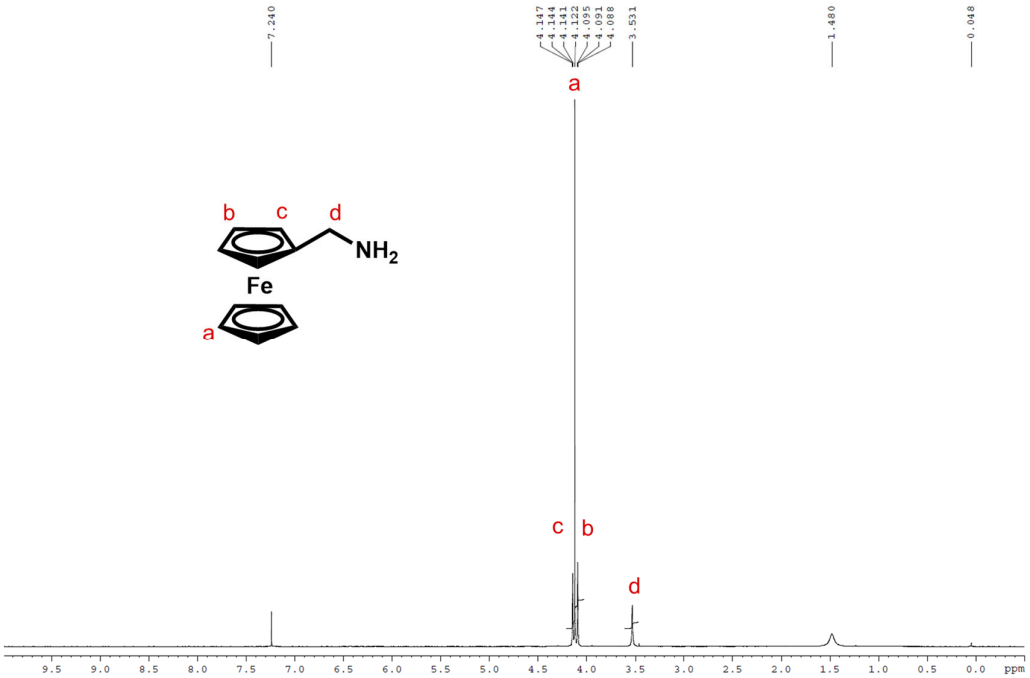

Fig. S3. ^{1}H NMR spectrum (500 MHz, $CDCl_3$, 24.9 °C (298 K)) of ferrocenemethylamine

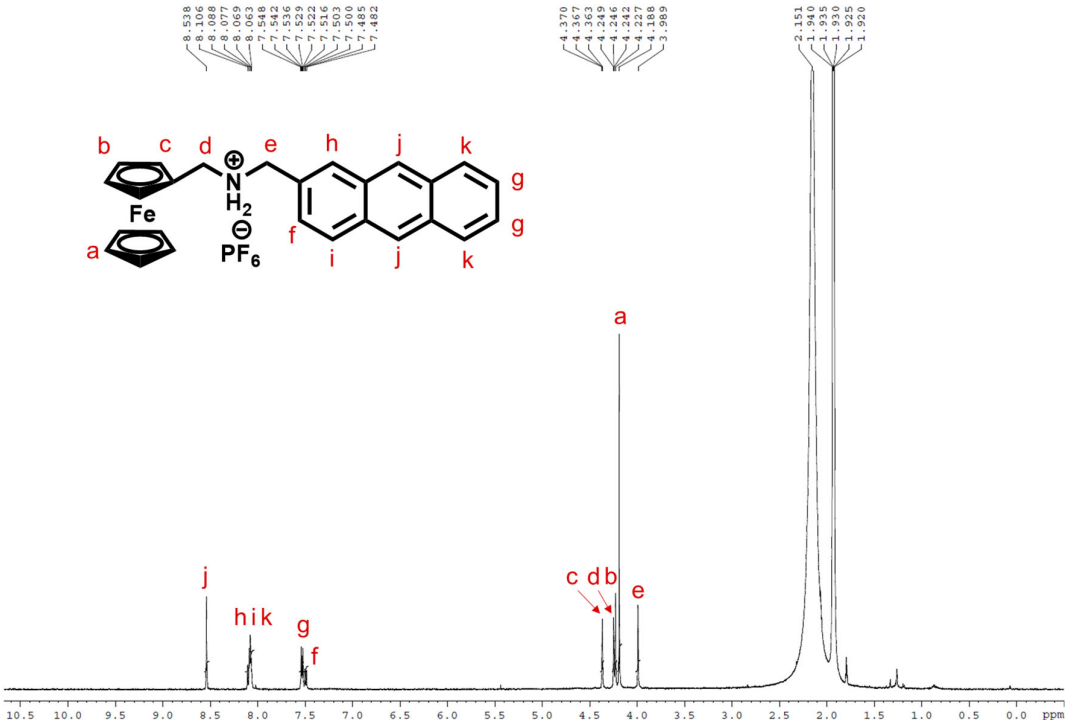

Fig. S4. ^{1}H NMR spectrum (500 MHz, CD_3CN, 24.9 °C (298 K)) of **A1**

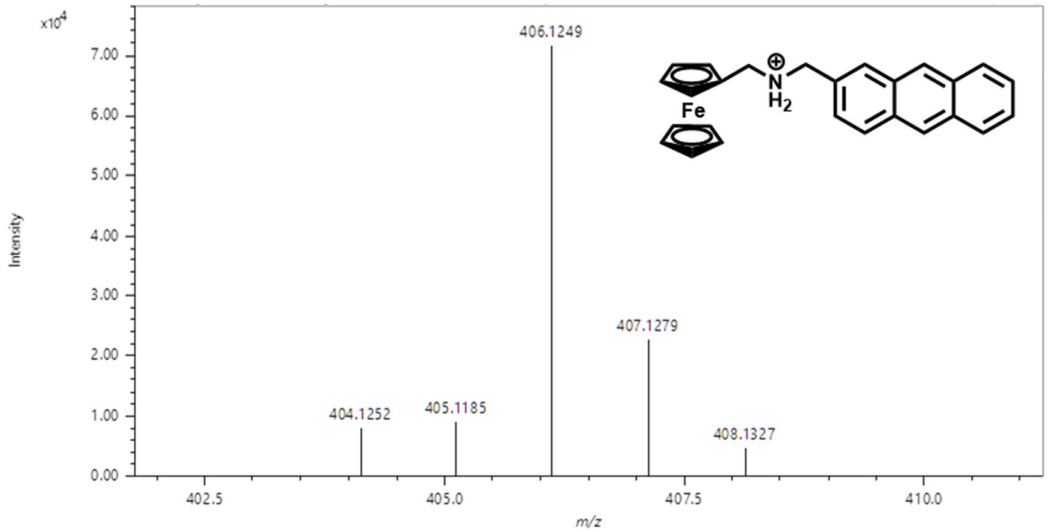

Fig. S5. High-resolution field desorption mass spectrum of **A1**. The major peak at *m*/*z* = 406.1249 corresponds to $[C_{26}H_{24}FeN]^+$ (calcd: 406.1252), with a mass error of 0.74 ppm.

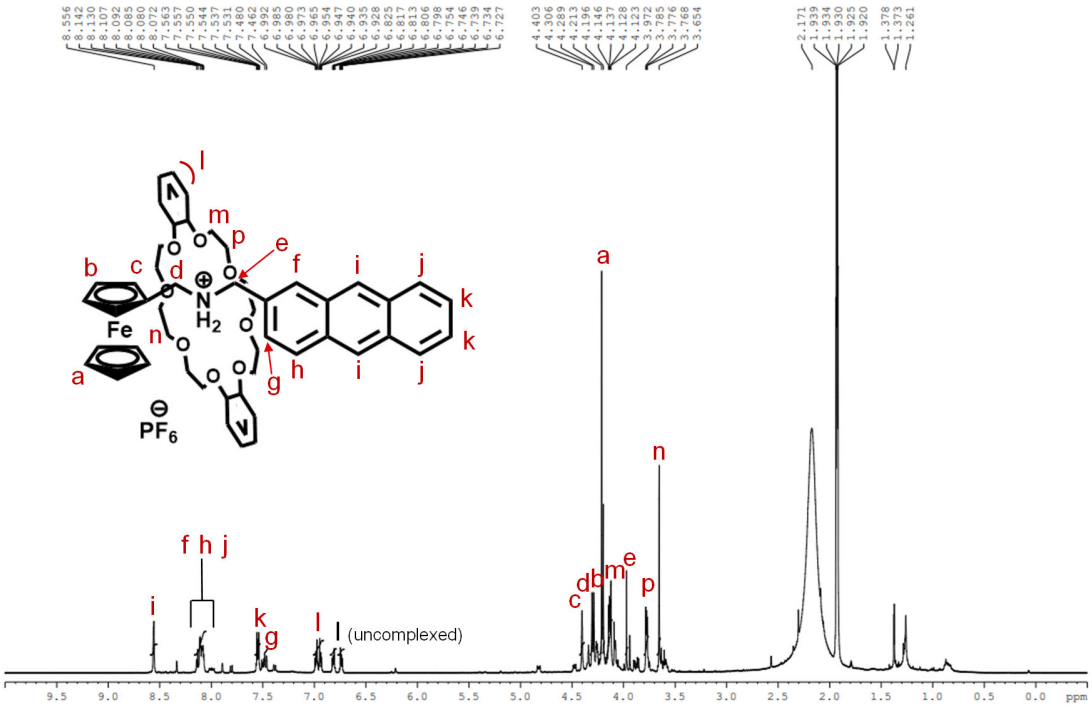

Fig. S6. ^{1}H NMR spectrum (500 MHz, CD_3CN, 24.9 °C (298 K)) of the **PR1**

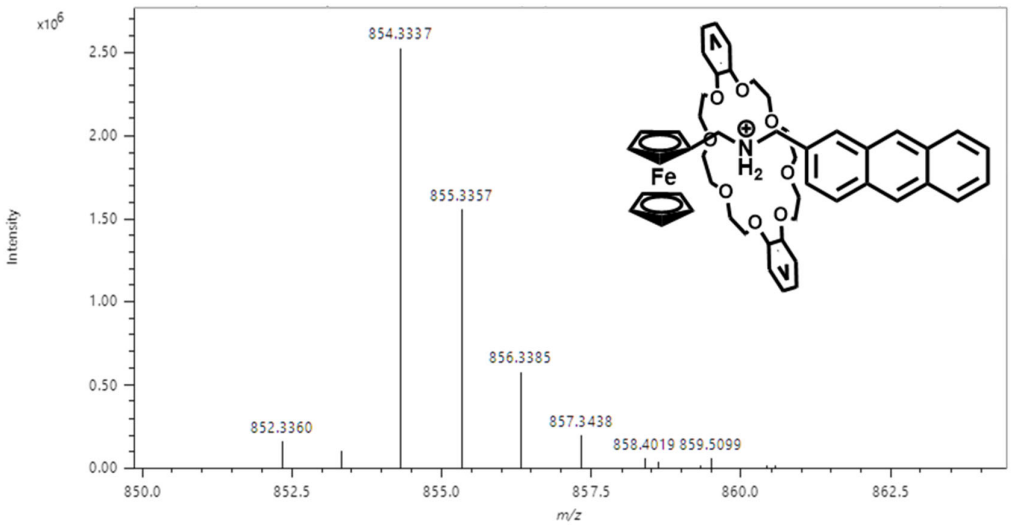

Fig. S7. High-resolution field desorption mass spectrum of **PR1**. The major peak at *m*/*z* = 854.3337 corresponds to $[C_{50}H_{56}FeNO_8]^+$ (calcd: 854.3350), with a mass error of 1.5 ppm.

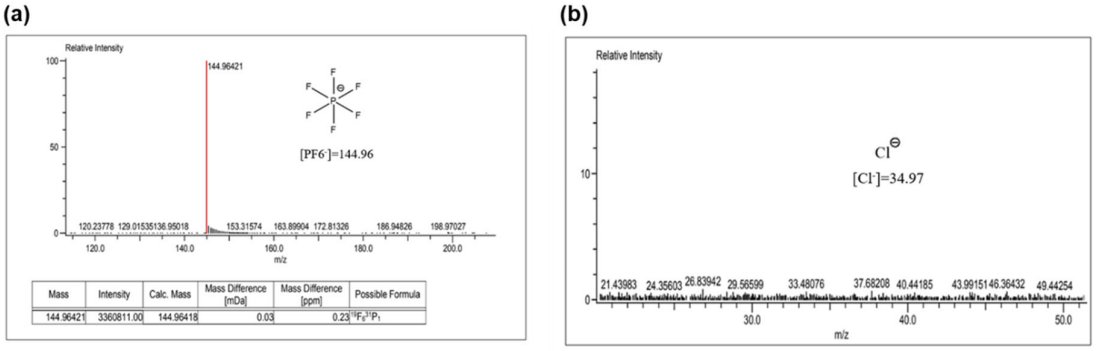

Fig. S8. ESI^- mass spectrum of of **PR1**. (a) The main peak at *m*/*z* = 144.9642 corresponds to $[PF_6^-]$ (calcd: 144.9642), with a mass error of 0.07 ppm. (b) The spectrum shows no signal corresponding to Cl^-, indicating its absence.

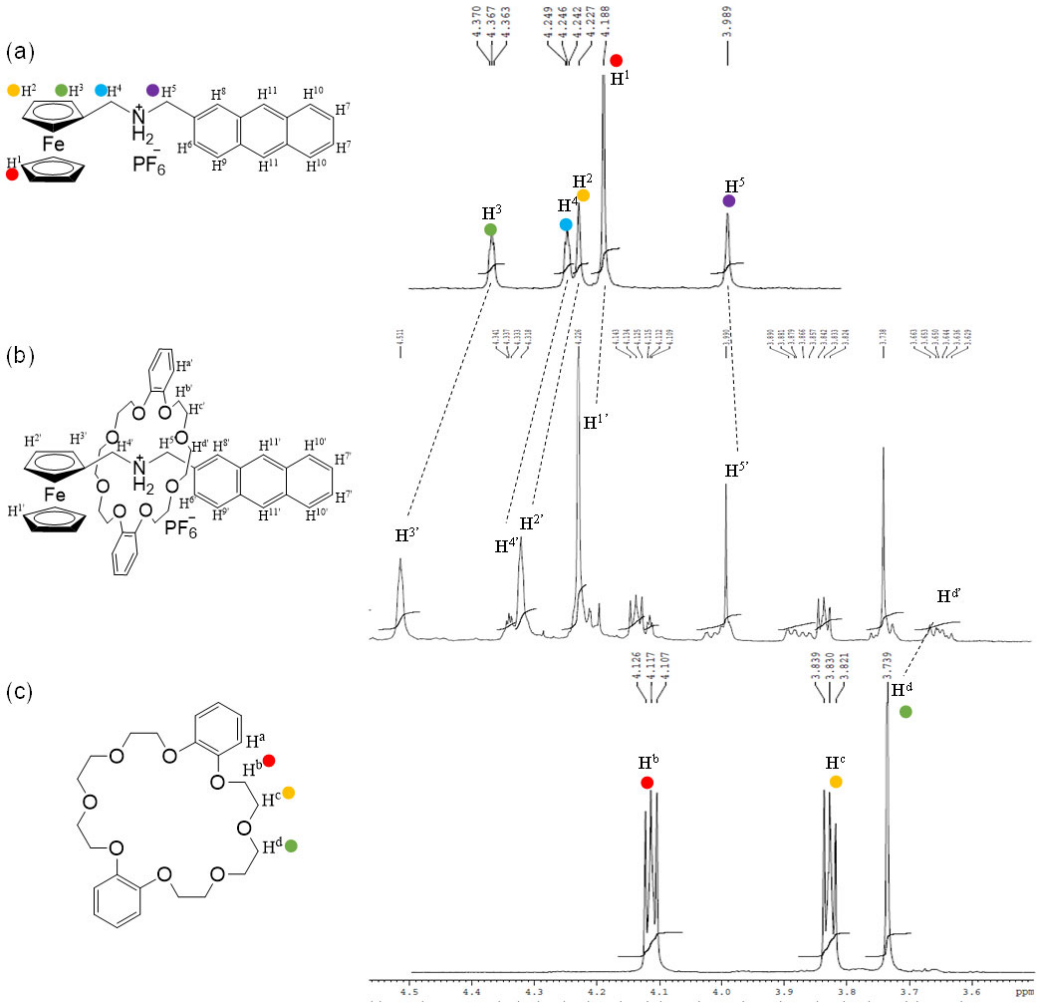

Fig. S9. ^{1}H NMR spectra (500 MHz, 24.9 °C (298 K), CD_3CN) in the chemical shift range of 3.5–4.5 ppm for (a) **A1**, (b) **PR1**, and (c) DB24C8.

Table S1. Summary of ^{1}H NMR (500 MHz, 24.9 °C (298 K), CD_3CN) chemical shift values for **A1**, DB24C8, and **PR1** in the range of 3.5–4.5 ppm.

Compound	Host (ppm)			Thread-Fc (ppm)		
	H^b	H^c	H^d	H^1	H^2, H^3	H^4, H^5
A1	-	-	-	4.19	4.23, 4.37	4.25, 3.98
DB24C8	4.12	3.83	3.74	-	-	-
PR1	4.11	3.85	3.65	4.22	4.31, 4.51	4.33, 3.97

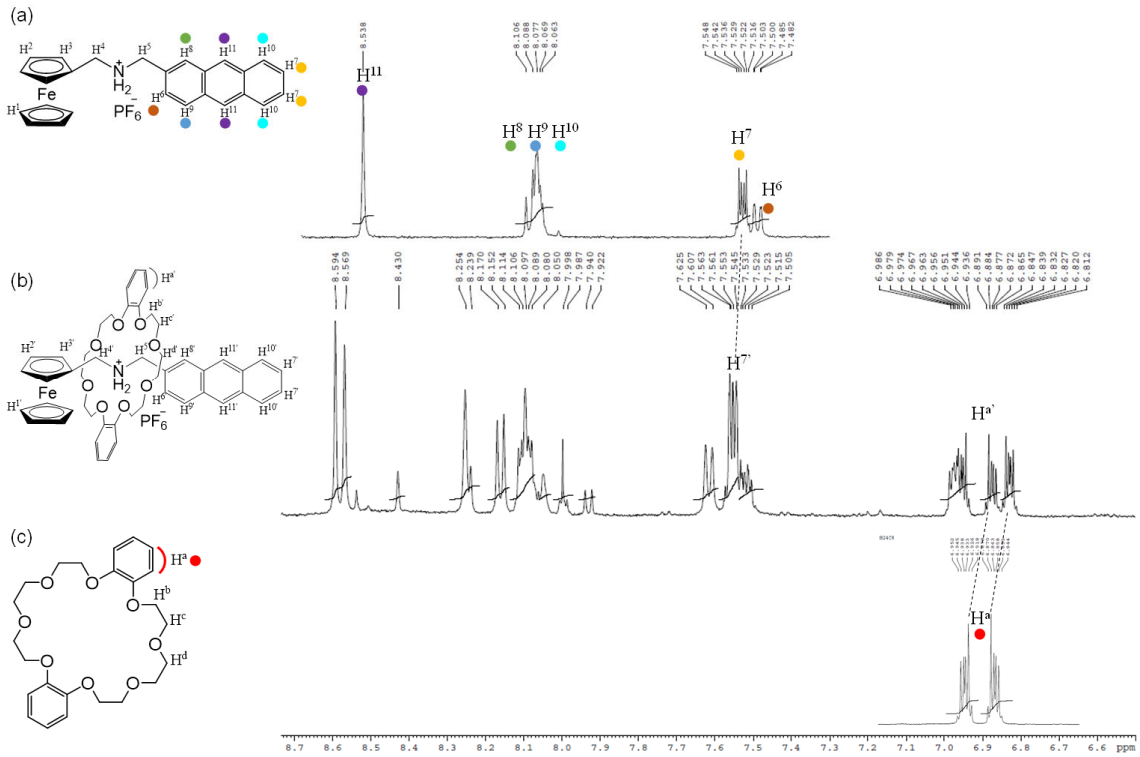

Fig. S10. ^{1}H NMR spectra (500 MHz, 24.9 °C (298 K), CD_3CN) in the chemical shift range of 6.5–8.6 ppm for (a) **A1**, (b) **PR1**, and (c) DB24C8.

Table S2. Summary of ^{1}H NMR (500 MHz, 24.9 °C (298 K), CD_3CN) chemical shift values for **A1**, DB24C8, and **PR1** in the range of 6.5–8.6 ppm

Compound	Host (ppm)	Thread-anthryl (ppm)			
	H^a	H^6	H^7	H^8, H^9, H^{10}	H^{11}
A1	-	7.48, 7.50	7.52-7.55	8.06-8.11	8.54
DB24C8	6.90	-	-	-	-
PR1	6.96	7.50, 7.53	7.53-7.56	8.08-8.17	8.57

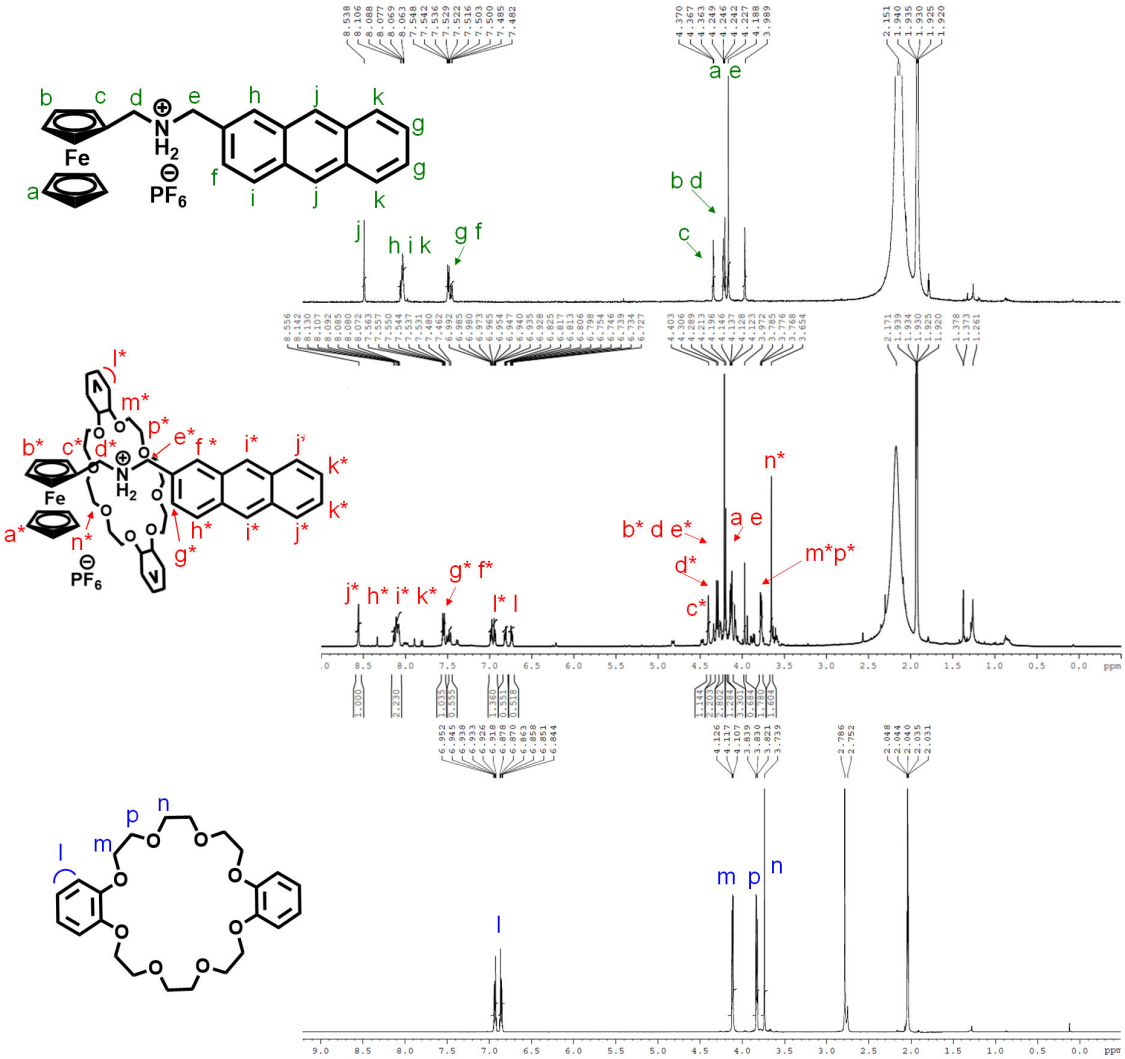

$$\textbf{Complex ratio} = \frac{[I*]}{[I]} = \frac{[1.36]}{[1.36+(0.55+0.52)]} = 0.56$$

Fig. S11. ^{1}H NMR spectra (500 MHz, 24.9 °C (298 K)) of **A1**, **PR1** and DB24C8 in $CDCl_3$:acetone-d_6 = 7:3 (vol/vol). The complexation ratio was estimated from the integration of the aromatic peaks of DB24C8 at 6.83–6.99 ppm (complexed) and 6.73–6.82 ppm (uncomplexed).

S2. Crystallographic Data

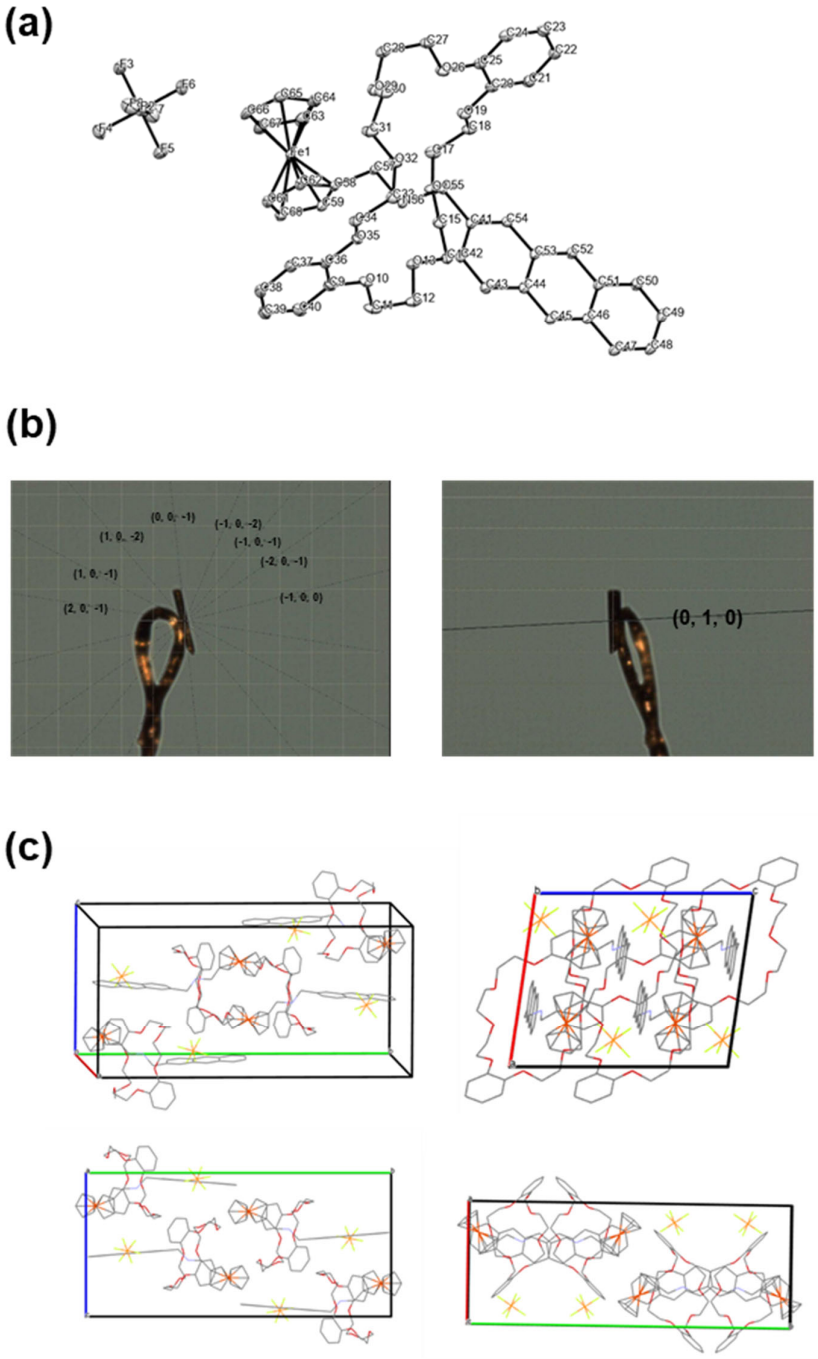

Fig. S12. (a) ORTEP drawing of **PR1** at –173.15 °C (100 K), showing 30% probability displacement ellipsoids. (b) Photos of the crystal, displaying the Miller indices of exposed surfaces. (c) Molecular alignment within the unit cell viewed along the *a*, *b*, and *c* crystallographic axes.

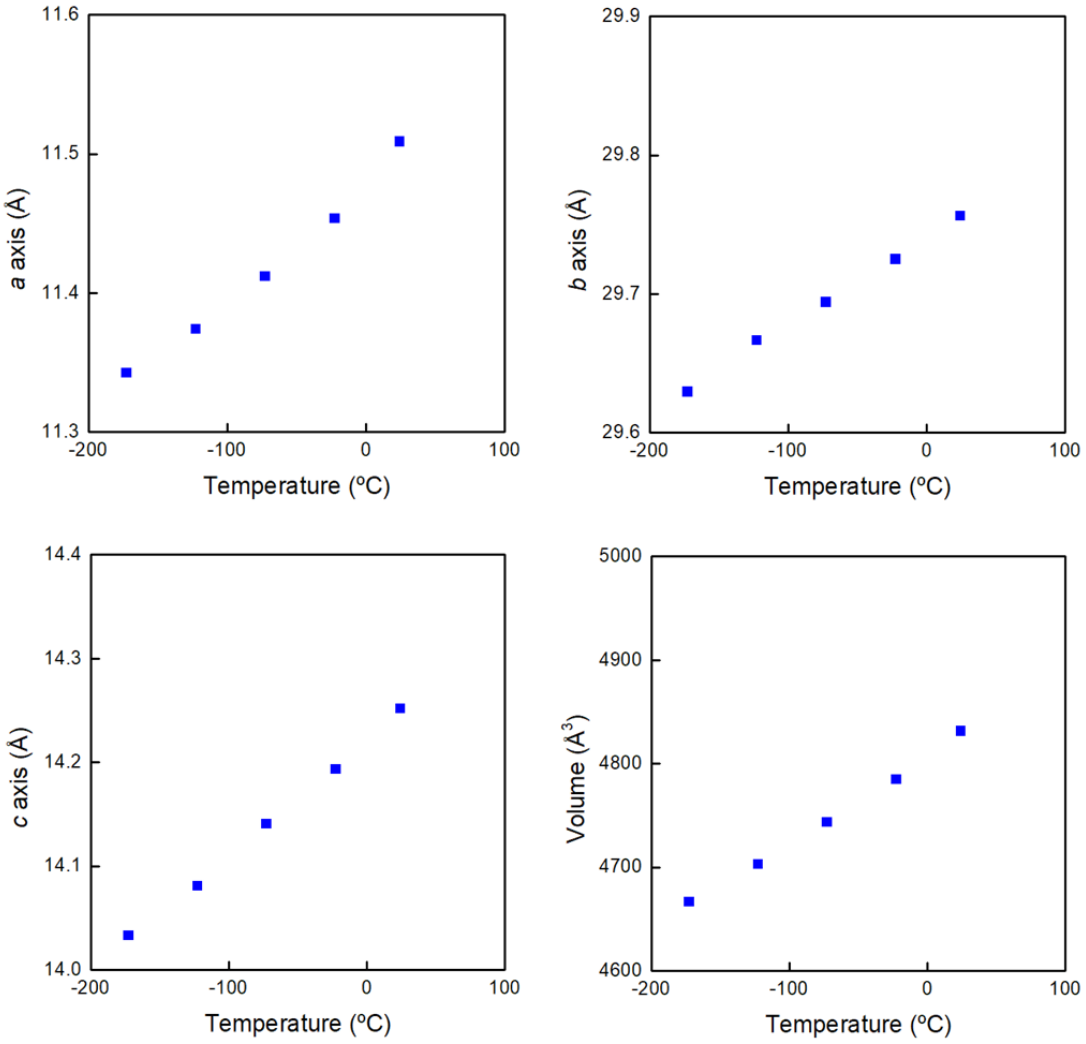

Fig. S13. Temperature-dependent unit cell parameters and volume of **PR1** obtained from single-crystal X-ray crystallography

Table S3. Crystal data and details of structure refinement of **PR1** at different temperatures.

Temperature/ °C (K)	–173 (100.01(10))	–123 (150.00(10))	–73 (200.00(10))
Molecular formula	$C_{50}H_{56}F_6FeNO_8P$	$C_{50}H_{56}F_6FeNO_8P$	$C_{50}H_{56}F_6FeNO_8P$
Molecular weight	999.77	999.77	999.77
Crystal system	Monoclinic	Monoclinic	Monoclinic
Space group	$P2_1/c$	$P2_1/c$	$P2_1/c$
a/ Å	11.3429(10)	11.3744(3)	11.4124(3)
b/ Å	29.6360(3)	29.6668(7)	29.6943(7)
c/ Å	14.0412(10)	14.0815(3)	14.1411(2)
α/ deg	90	90	90
β/ deg	98.3000(10)	98.170(2)	98.114(2)
γ/ deg	90	90	90
Volume/ $Å^3$	4667.14(7)	4703.5(2)	4744.18(17)
Z	4	4	4
μ(MoKα)/ mm^{-1}	3.600	3.572	3.542
F(000)	2088.0	2088.0	2088.0
Density/ g cm^{-3}	1.423	1.412	1.400
Crystal size/ mm	0.13 x 0.03 x 0.02	0.12 x 0.07 x 0.03	0.08 x 0.04 x 0.03
Reflections collected	51830	30032	38027
Independent reflections	8307	8354	8407
R	0.0384	0.0564	0.0576
R_w	0.0998	0.1466	0.1477
GOF	1.070	1.041	1.030

Table S4. Crystal data and details of structure refinement of **PR1** at different temperatures.

Temperature/ °C (K)	–23 (250.00(10))	24 (297.00(10))	47 (320.00(10))
Molecular formula	$C_{50}H_{56}F_6FeNO_8P$	$C_{50}H_{56}F_6FeNO_8P$	$C_{50}H_{56}F_6FeNO_8P$
Molecular weight	999.77	999.77	999.77
Crystal system	Monoclinic	Monoclinic	Monoclinic
Space group	$P2_1/c$	$P2_1/c$	$P2_1/c$
a/ Å	11.4540(4)	11.5093(6)	11.5366(6)
b/ Å	29.7253(7)	29.7566(13)	29.8004(11)
c/ Å	14.1940(3)	14.2524(4)	14.2802(5)
α/ deg	90	90°	90°
β/ deg	98.014(3)	98.146(2)°	98.105(4)
γ/ deg	90	90°	90°
Volume/ $Å^3$	4785.5(2)	4831.9(4)	4860.4(3)
Z	4	4	4
μ(MoKα)/ mm^{-1}	3.511	3.477	3.457
F(000)	2088.0	2088.0	2088.0
Density/ g cm^{-3}	1.388	1.374	1.366
Crystal size/ mm	0.12 x 0.07 x 0.03	0.08 x 0.04 x 0.03	0.08 x 0.04 x 0.03
Reflections collected	31389	38291	32262
Independent reflections	8503	8557	8645
R	0.0673	0.0786	0.0806
R_w	0.1727	0.2062	0.2075
GOF	1.041	0.990	1.009

Due to substantial deterioration in data quality above 77 °C (350 K), detailed structural analysis is based on the crystallographic data obtained below 47 °C (320 K).

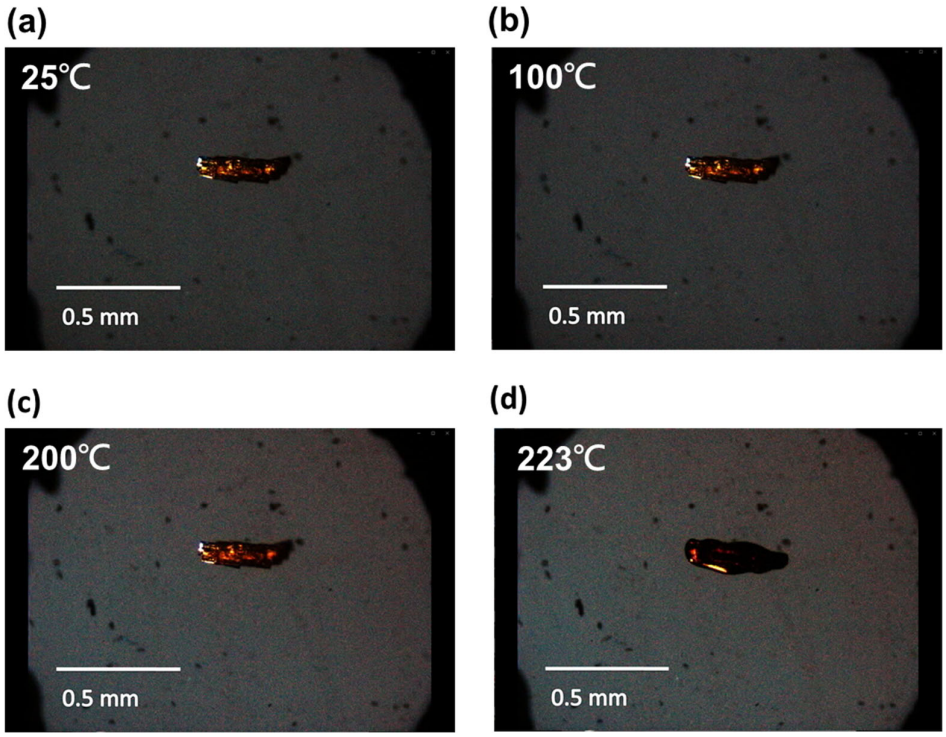

Fig. S14. Polarized optical micrographs of a **PR1** crystal at (a) 25 °C, (b) 100 °C, (c) 200 °C, and (d) 223 °C.

Table S5. Retardation, thickness and average birefringence of **PR1**

Crystal	*R* (nm)	*d* (μm)	Δ*n*	Avg. Δ*n*
#1	539.24	8.50	0.063	0.063
	496.84	7.92	0.063	
	465.54	7.37	0.063	
#2	805.51	12.26	0.066	0.065
	768.86	11.90	0.065	
	734.18	11.47	0.064	
#3	298.38	4.37	0.068	0.068
	311.24	4.55	0.068	
	326.16	4.75	0.069	

S3. Hirshfeld Surface Analysis

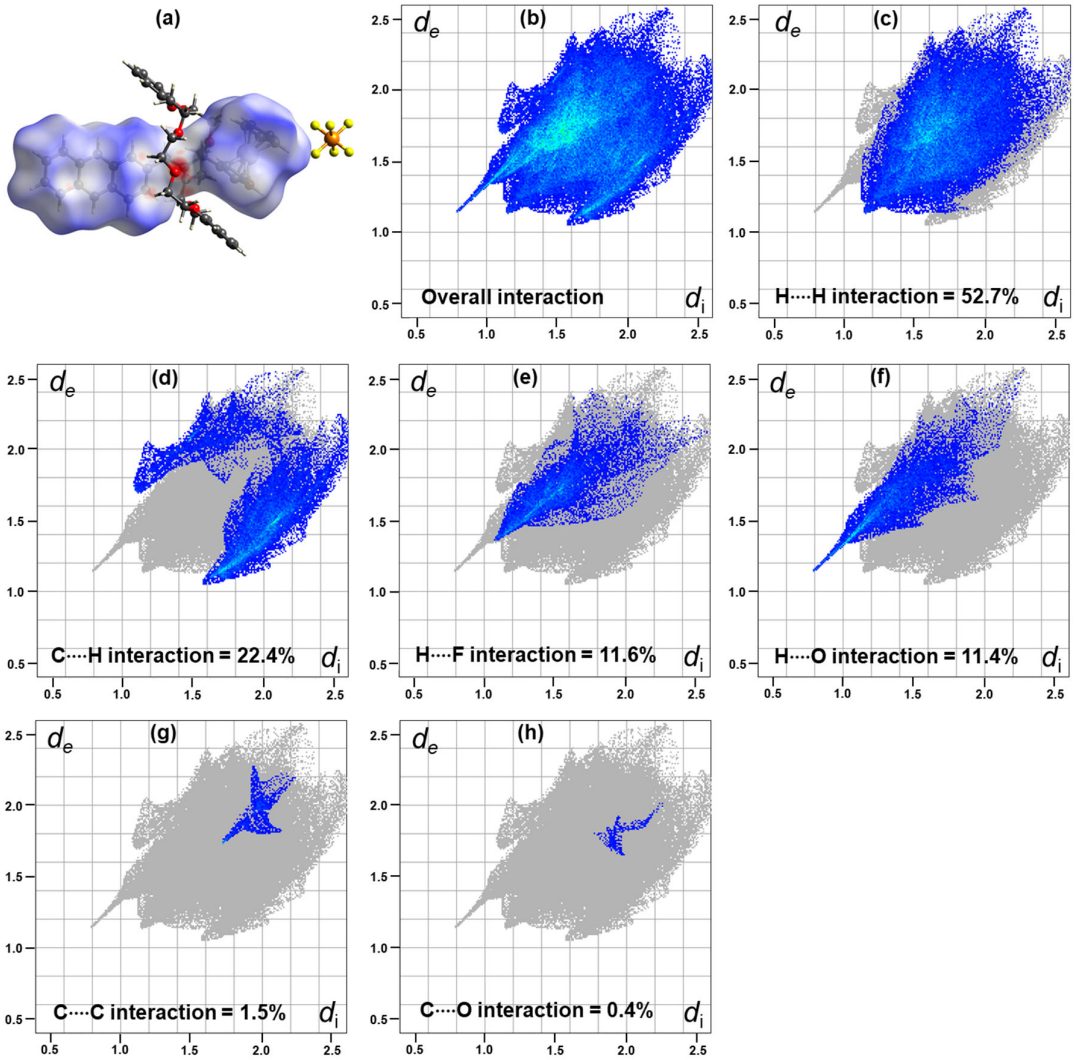

Fig. S15. (a) Hirshfeld surface (HS) mapped over d_{norm} for the axle molecule in **PR1** at –173 °C (100 K). (b) 2D fingerprint plot of overall intermolecular interactions. (c–h) 2D fingerprint plots of specific interaction types for the axle molecule in **PR1** at –173 °C.

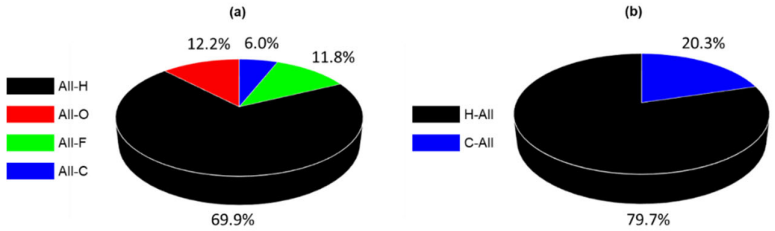

Fig. S16. Percentage contributions of intermolecular interactions in **PR1** at –173 °C (100 K), calculated from HS analysis: (a) interactions between all atoms within the HS and an external atom, and (b) interactions between an internal atom and all surrounding atoms outside the HS.

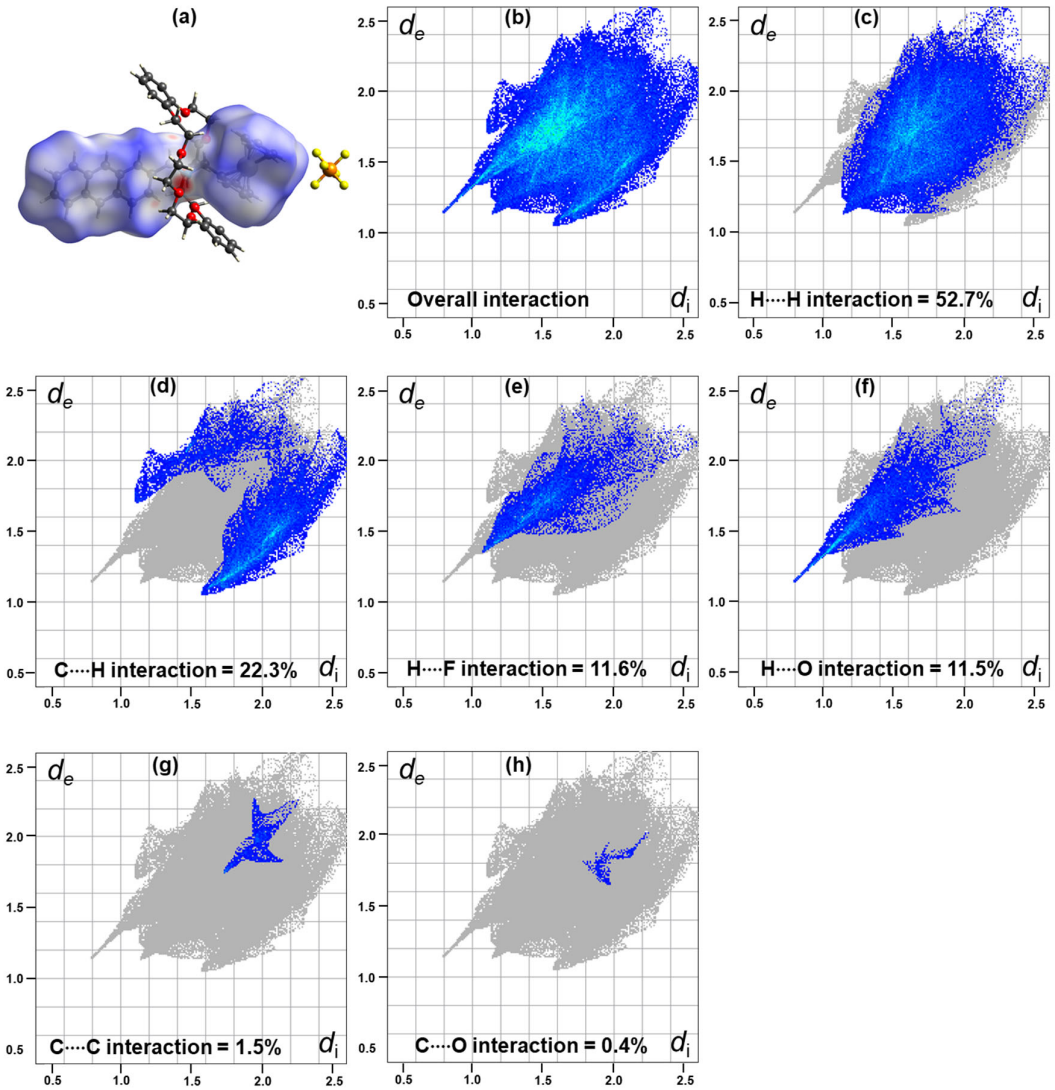

Fig. S17. (a) HS mapped over d_{norm} for the axle molecule in **PR1** at 47 °C (320 K). (b) 2D fingerprint plot of overall intermolecular interactions. (c–h) 2D fingerprint plots of specific interaction types for the axle molecule in **PR1** at 47 °C.

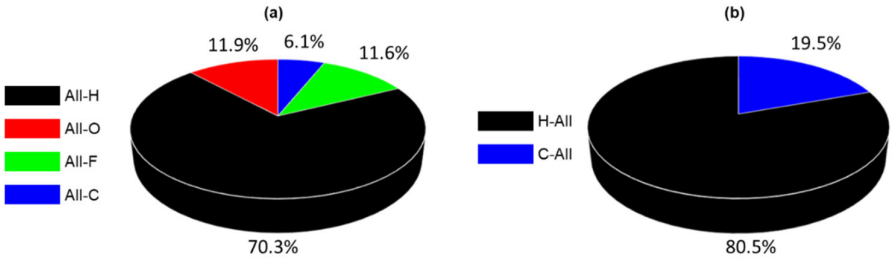

Fig. S18. Percentage contributions of intermolecular interactions in **PR1** at 47 °C (320 K), calculated from HS analysis: (a) interactions between all atoms within the HS and an external atom, and (b) interactions between an internal atom and all surrounding atoms outside the HS.

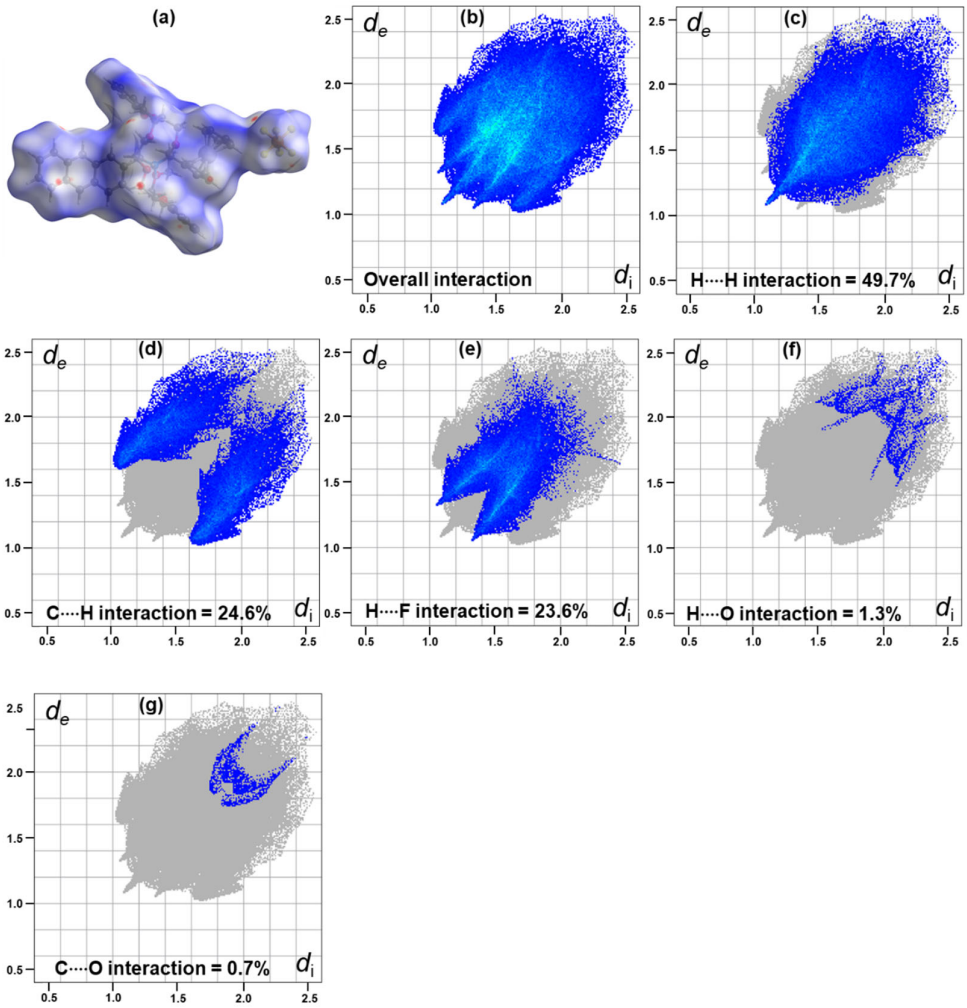

Fig. S19. (a) HS plotted over d_{norm} for **PR1** under –173 °C (100 K). 2D fingerprint plot for (b) overall interactions and (c-g) individual interactions in **PR1** under –173 °C.

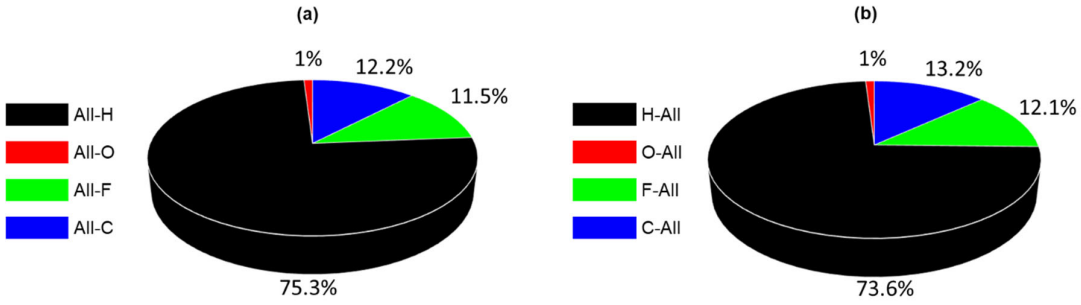

Fig. S20. Percentage contributions of intermolecular interactions in **PR1** at –173 °C (100 K) based on HS analysis: (a) interactions between all atoms within the HS and a single external atom, and (b) interactions between a single internal atom and all surrounding atoms outside the HS.

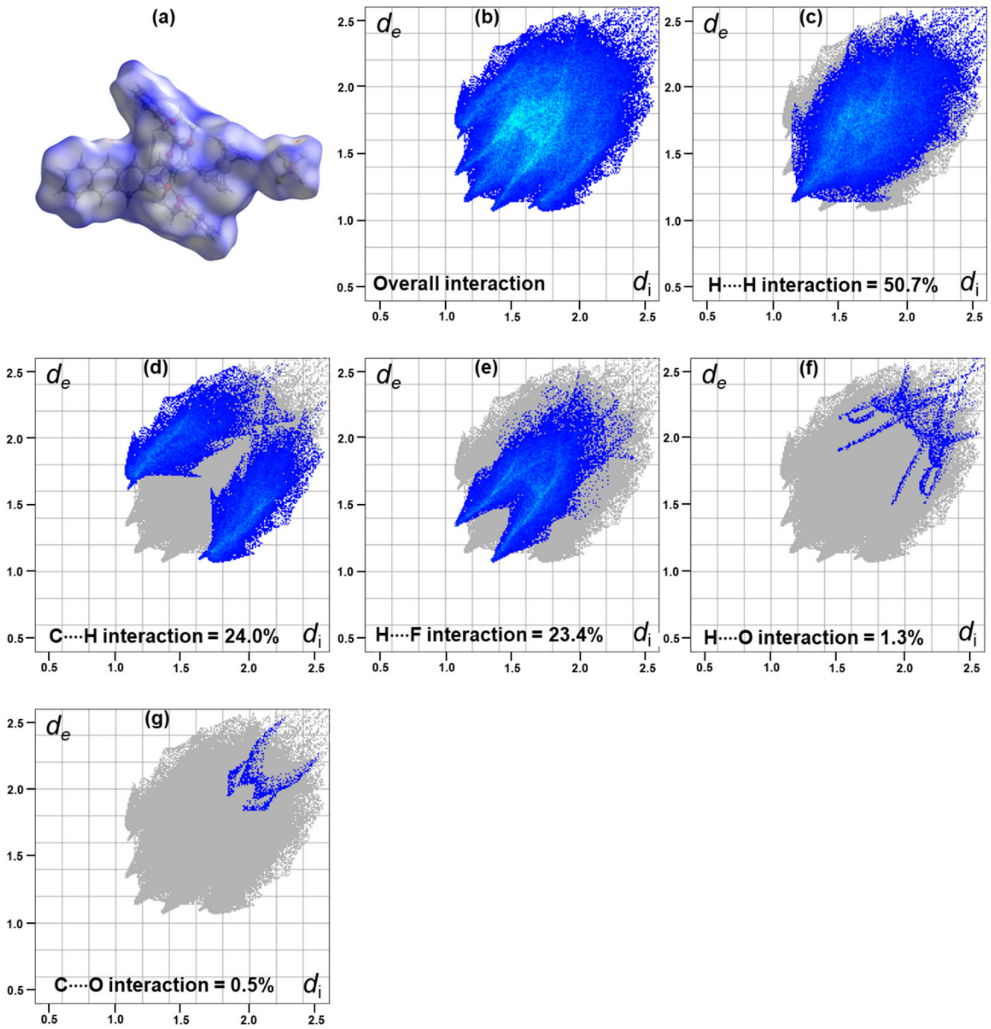

Fig. S21. (a) HS plotted over d_{norm} for **PR1** under 47 °C (320 K). 2D fingerprint plot for (b) overall interactions and (c-g) individual interactions in **PR1** under 46.85 °C.

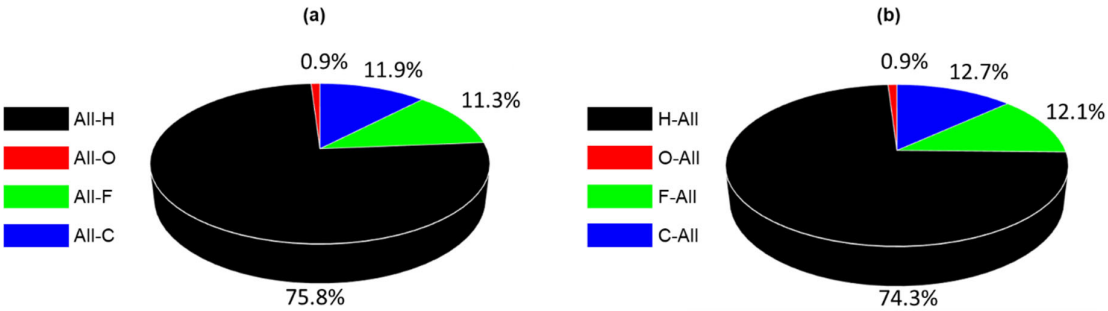

Fig. S22. Percentage contributions of intermolecular interactions in **PR1** at 47 °C (320 K) based on HS analysis: (a) interactions between all atoms within the HS and a single external atom, and (b) interactions between a single internal atom and all surrounding atoms outside the HS.

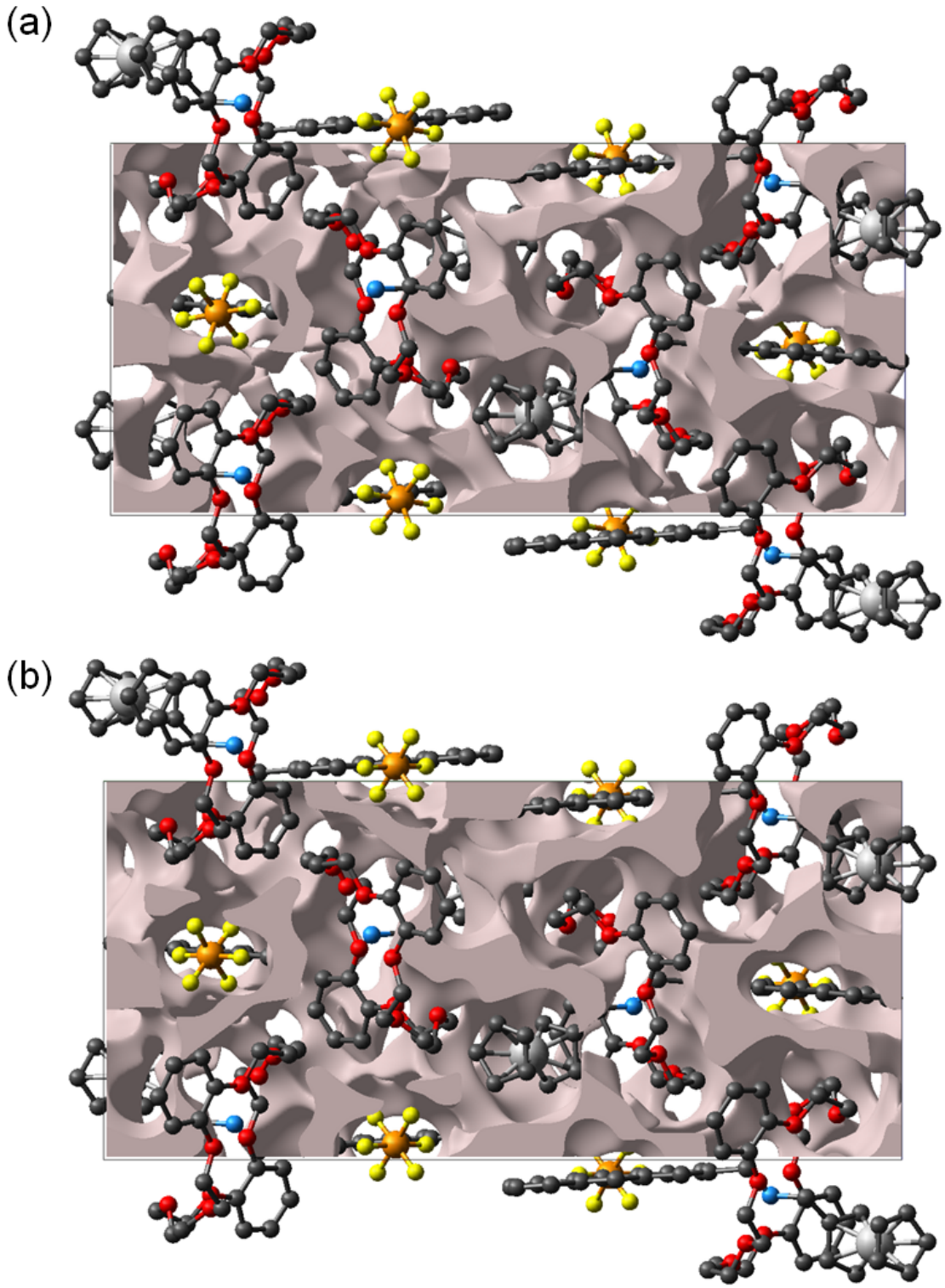

Fig. S23. Graphical representation of voids in the crystal packing of **PR1** at (a) –173 °C and (b) 47 °C.

S6. Film Preparation and Characterization

Table S6. Concentration of dopants in PBMA films

	PBMA	Axle	Ring	Complex or compound	Solvent
Ferrocene (7 mol%)	30 mg (0.211 mmol)	—	—	0.016 mmol	$CHCl_3$ (500 μL)
A1-PBMA (7 mol%)	30 mg (0.211 mmol)	8.816 mg (0.016 mmol)	—	0.016 mmol	$CHCl_3$ and acetone =1:1 (500 μL)
PR1-PBMA (7 mol%)	30 mg (0.211 mmol)	8.816 mg (0.016 mmol)	7.168 mg (0.016 mmol)	0.016 mmol	$CHCl_3$ and acetone =1:1 (500 μL)
Cr.PR1-PBMA (7 mol %)	9.38 mg (0.066 mmol)	—	—	5 mg (0.005 mmol)	Ether (300 μL)
Cr.PR2-PBMA (7 mol %)	16.43 mg (0.116 mmol)	—	—	8 mg (0.0088 mmol)	Ether (400 μL)

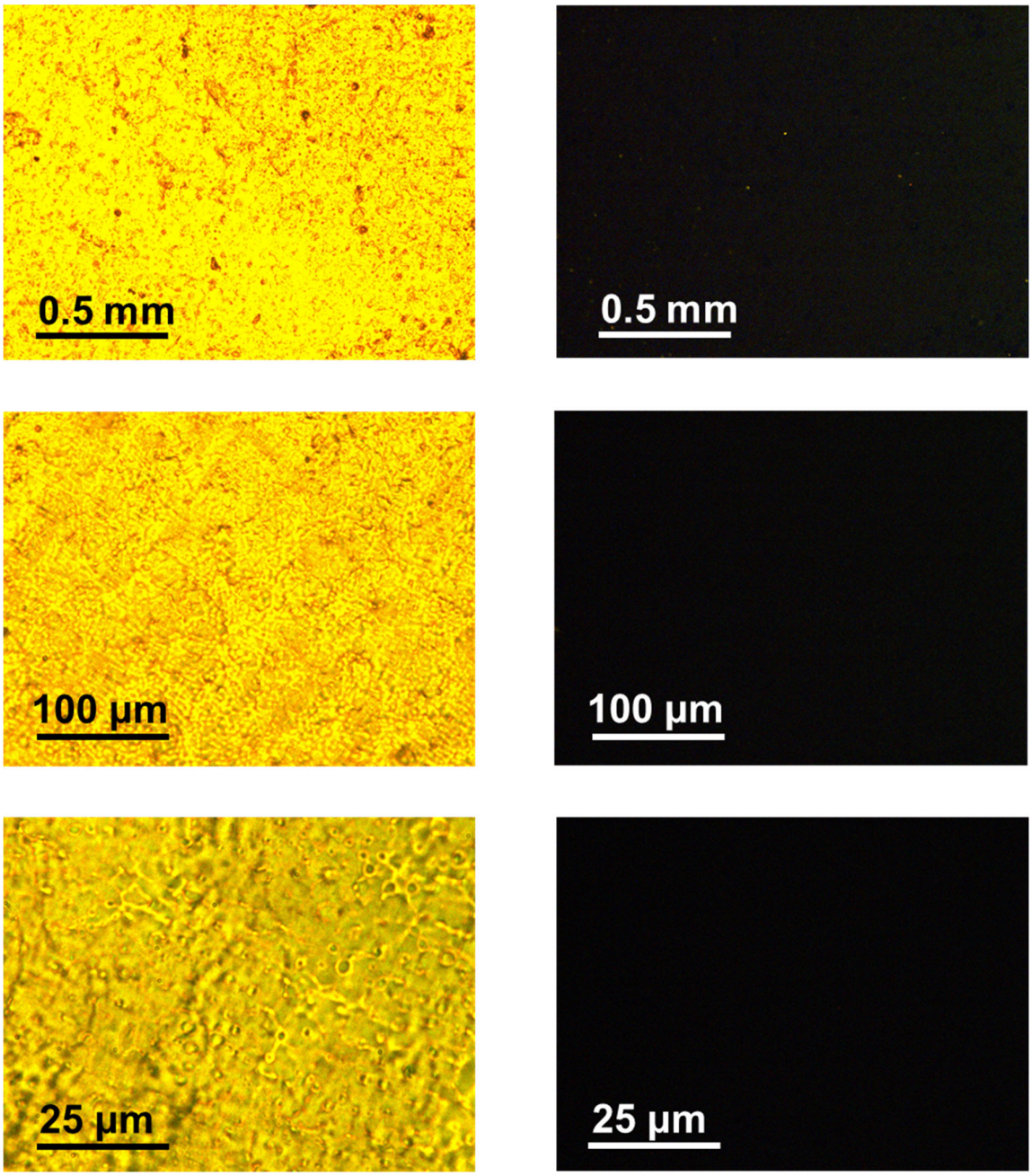

Fig. S24. Optical micrographs of **PR1-PBMA** at different magnifications under (left) non-polarized and (right) polarized light.

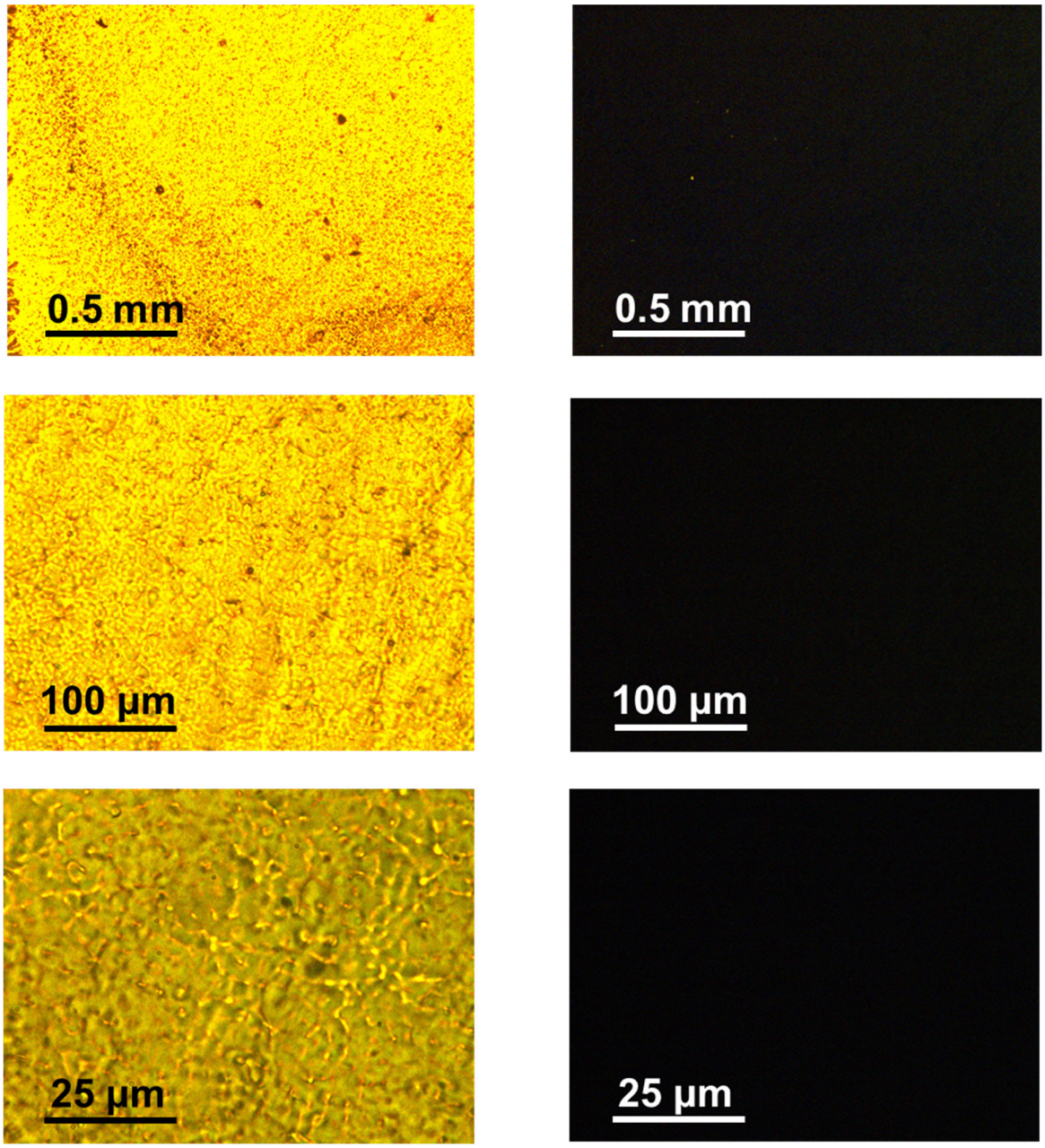

Fig. S25. Optical micrographs of **A1-PBMA** at different magnifications under (left) non-polarized and (right) polarized light.

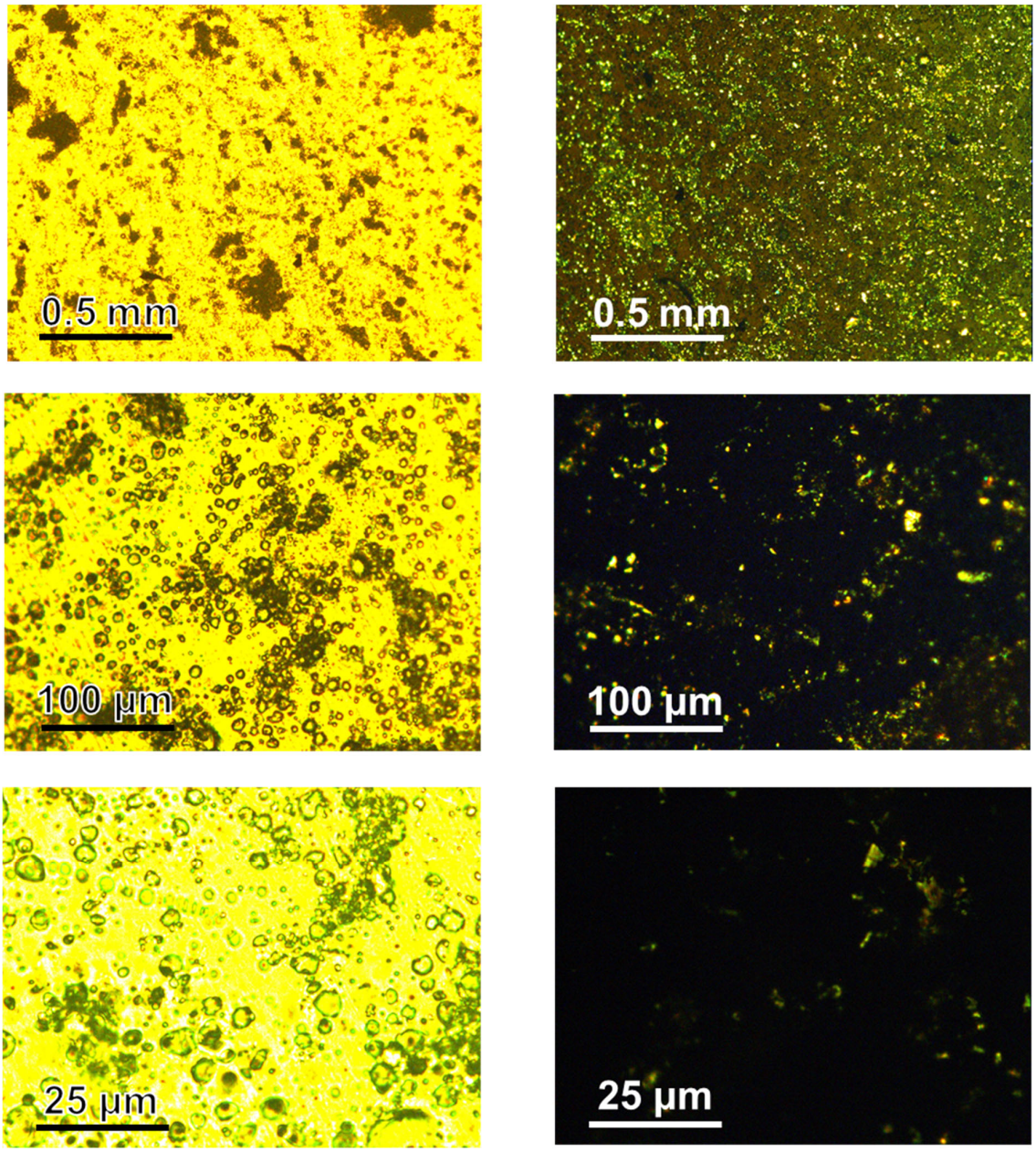

Fig. S26. Optical micrographs of **Cr.PR1-PBMA** at different magnifications under (left) non-polarized and (right) polarized light.

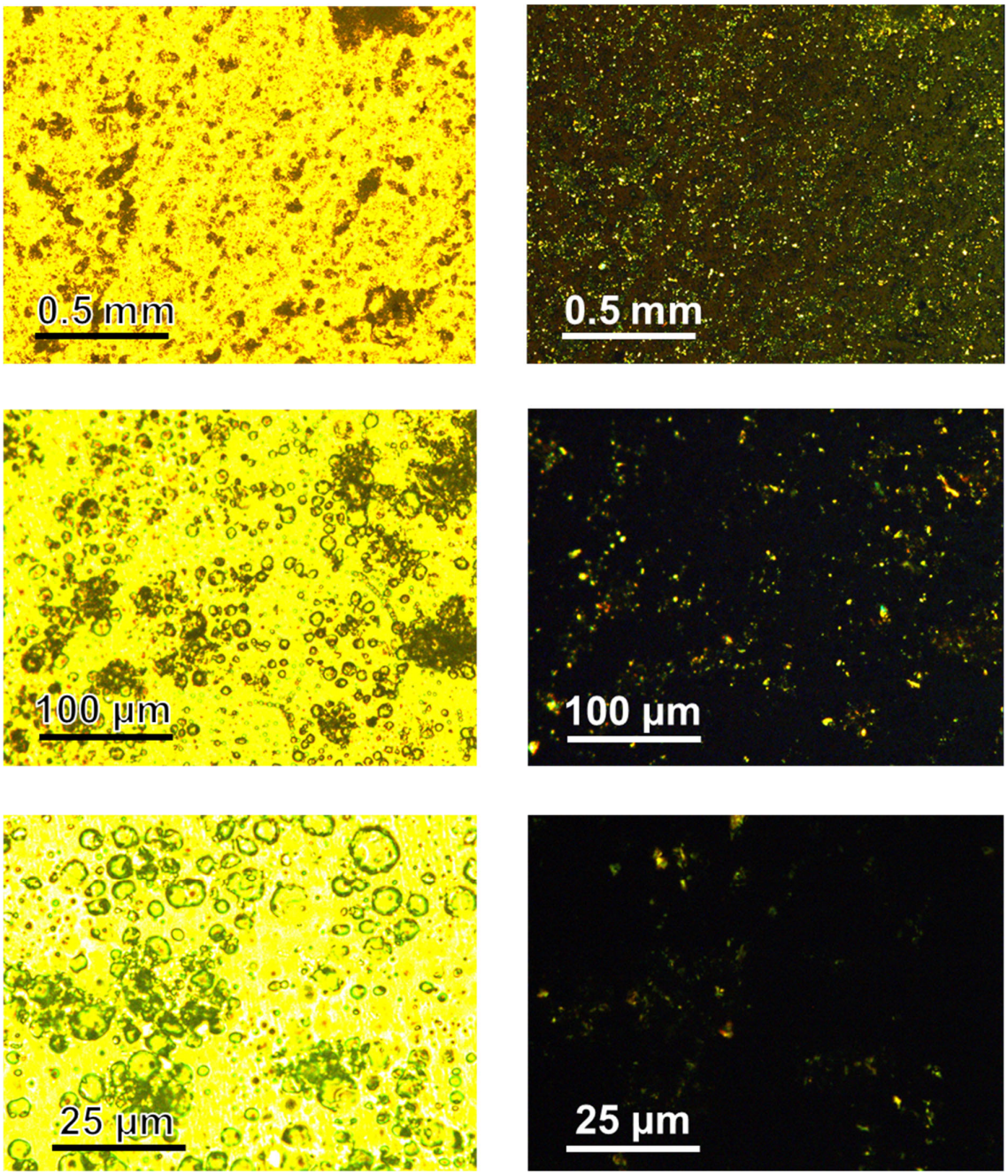

Fig. S27. Optical micrographs of **Cr.PR2-PBMA** at different magnifications under (left) non-polarized and (right) polarized light.

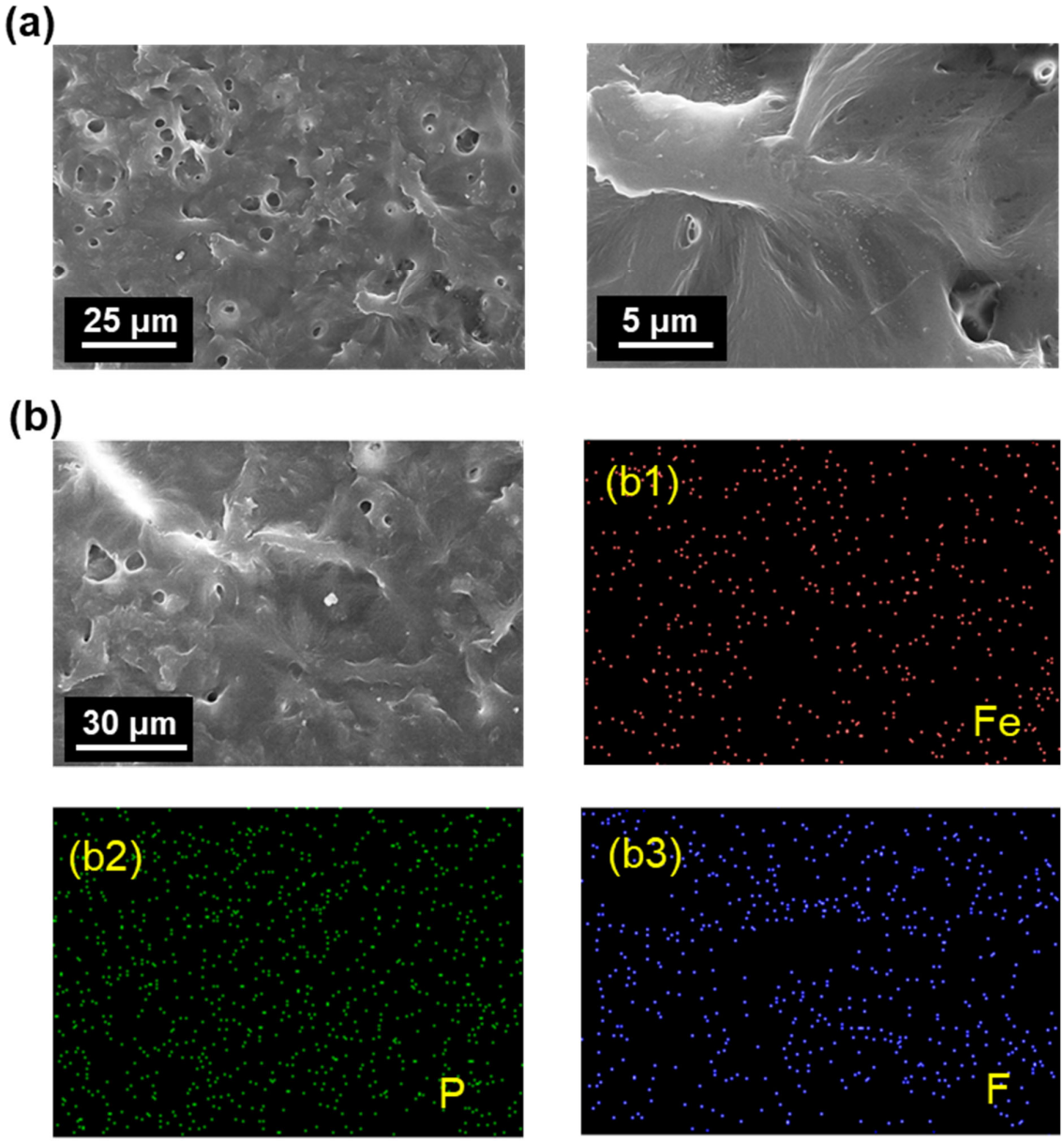

Fig. S28. (a) SEM image of **PR1-PBMA**. (b) EDX elemental mapping of **PR1-PBMA** showing distributions of (b1) Fe, (b2) P, and (b3) F.

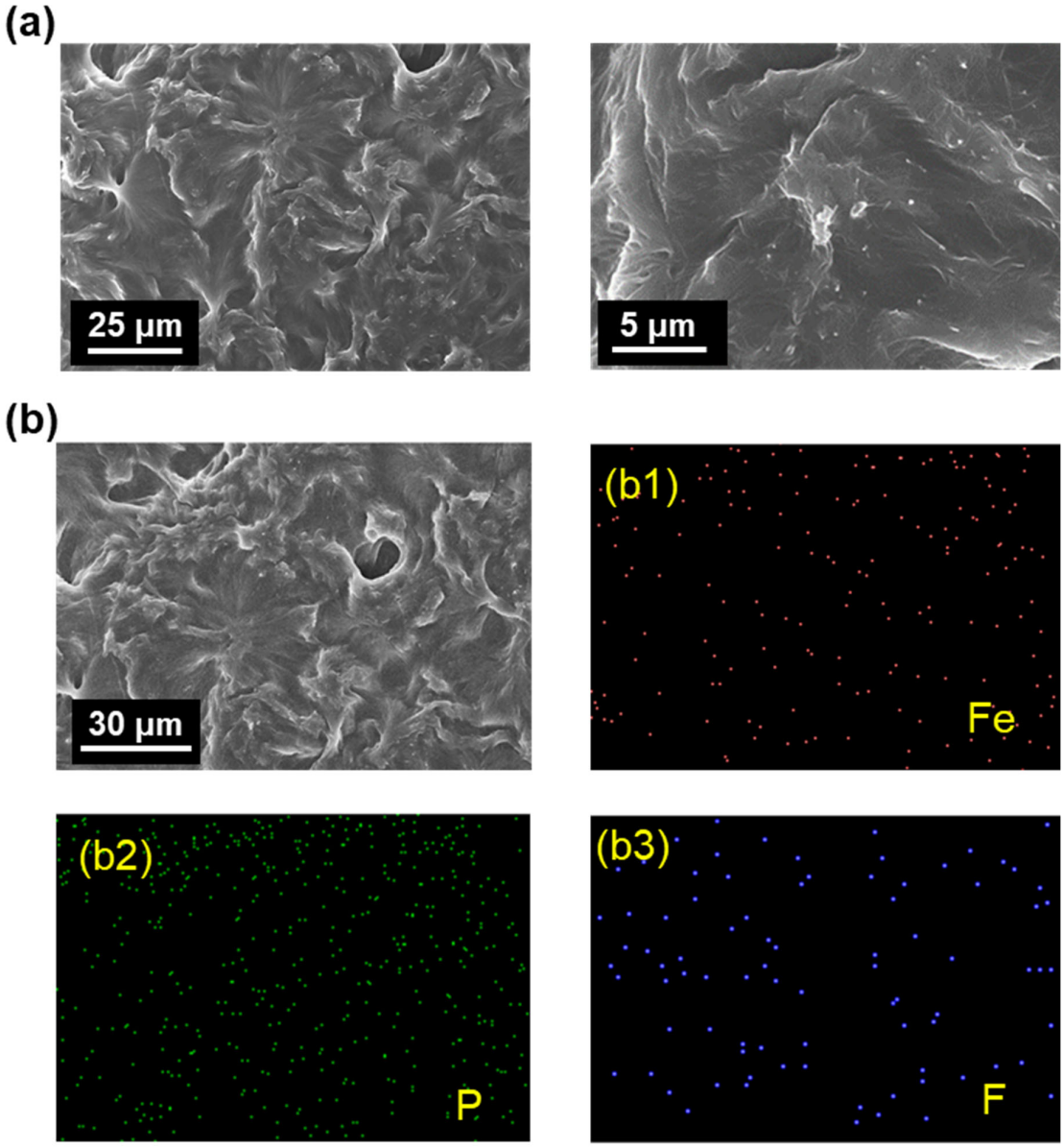

Fig. S29. (a) SEM image of **A1-PBMA**. (b) EDX elemental mapping of **A1-PBMA** showing distributions of (b1) Fe, (b2) P, and (b3) F.

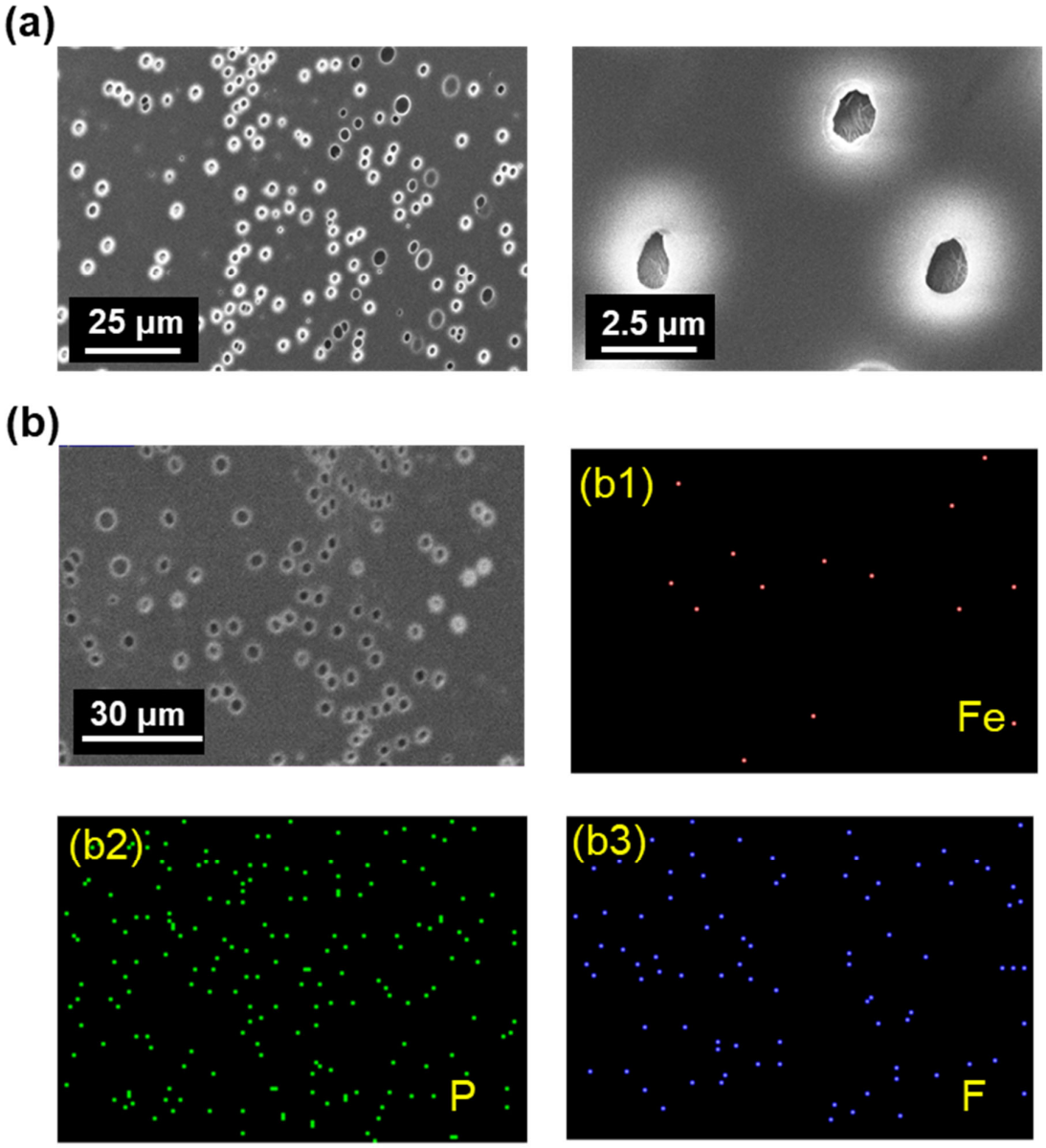

Fig. S30. (a) SEM image of **Cr.PR1-PBMA**. (b) EDX elemental mapping of **Cr.PR1-PBMA** showing distributions of (b1) Fe, (b2) P, and (b3) F.

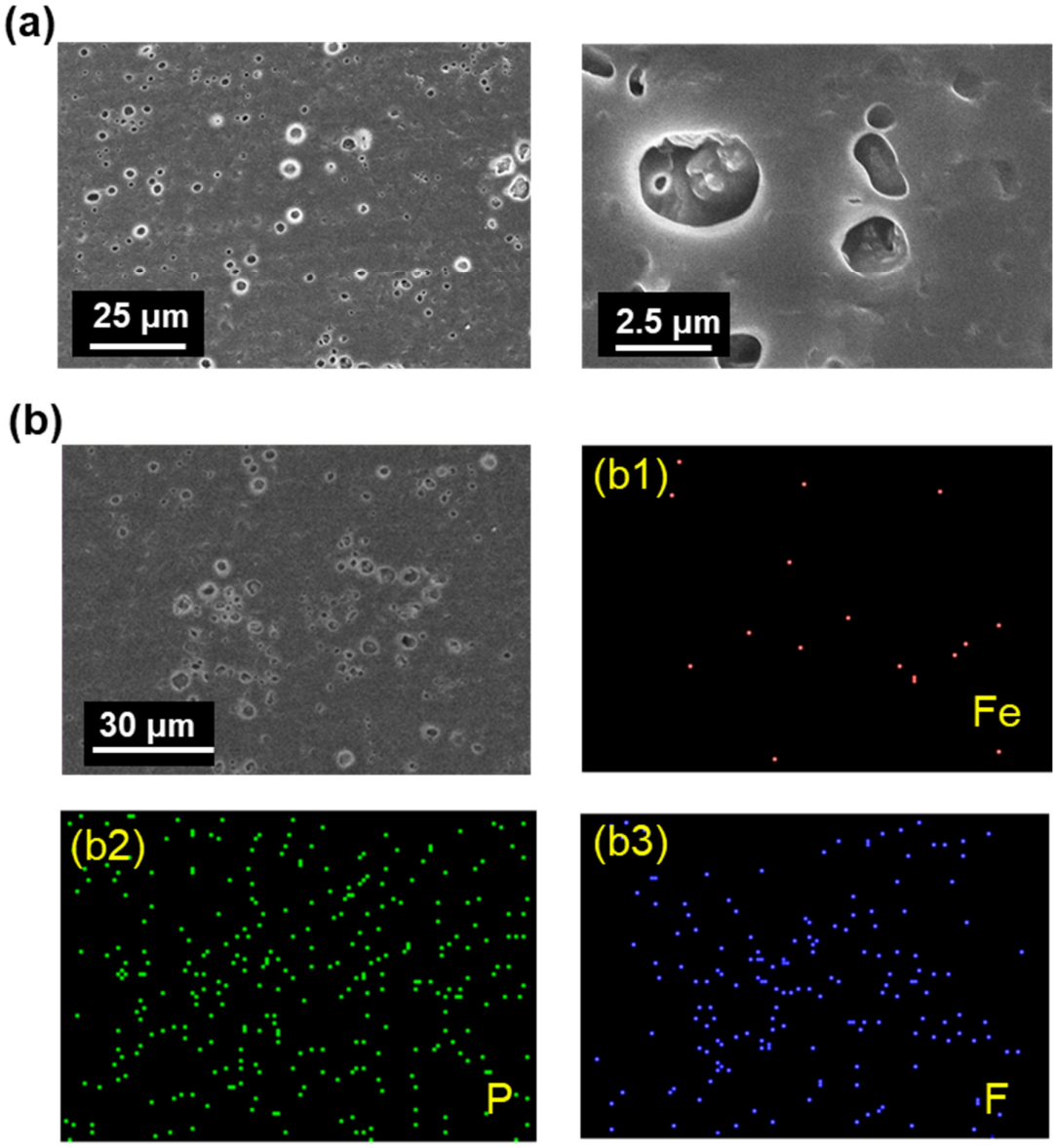

Fig. S31. (a) SEM image of **Cr.PR2-PBMA**. (b) EDX elemental mapping of **Cr.PR2-PBMA** showing distributions of (b1) Fe, (b2) P, and (b3) F.

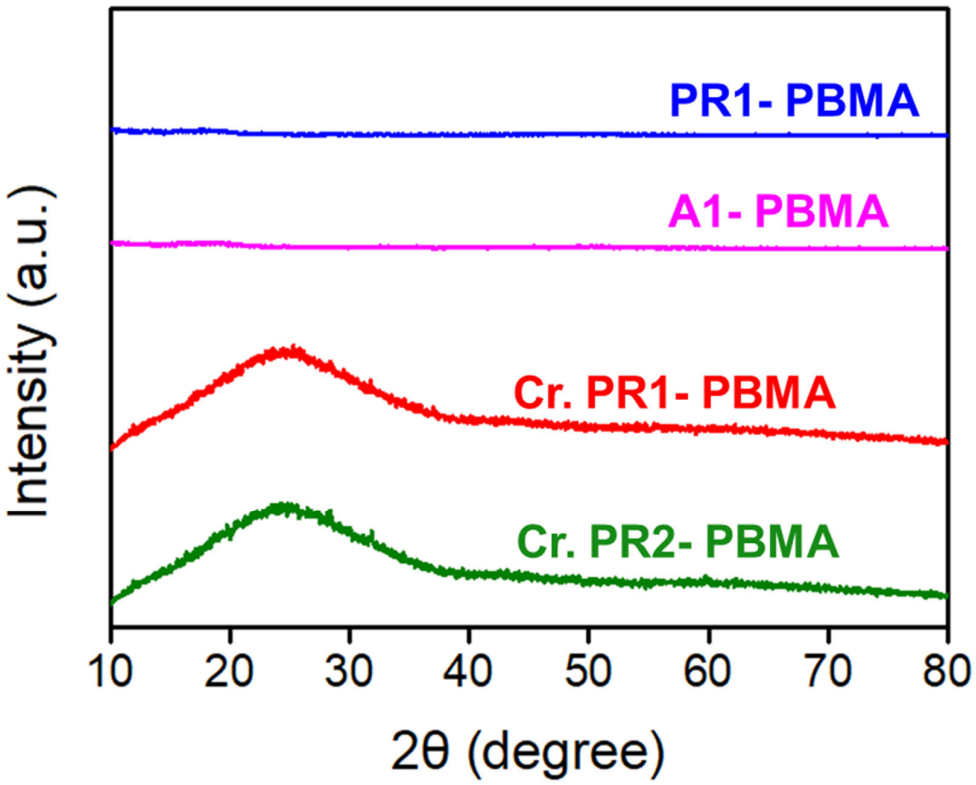

Fig. S32. XRD patterns of PBMA films

S5. Photoluminescence properties

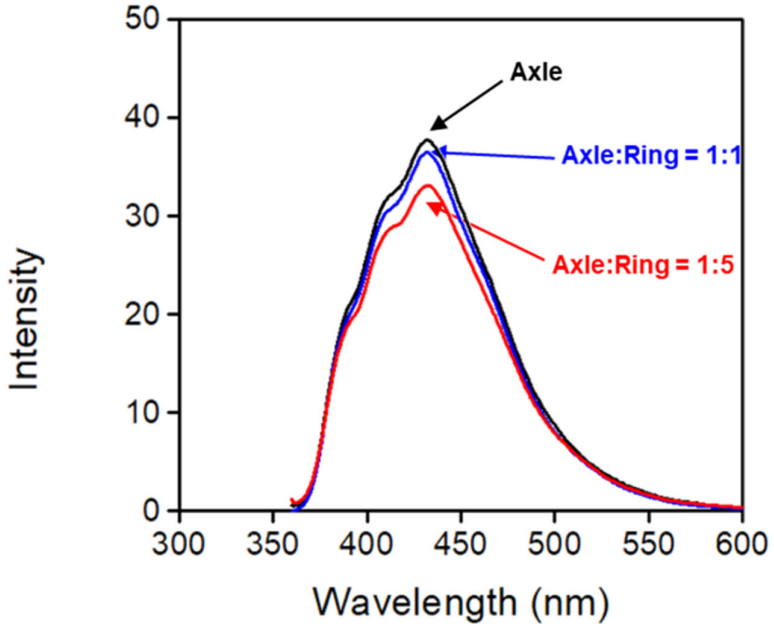

Fig. S33. Photoluminescence spectra of **A1** (13 ppm in acetone) with varying DB24C8 ratios

Table S7. Photoluminescence properties of **A1** with varying DB24C8 ratios in acetone.

Axle:Ring	$\lambda_{UV\text{-}VIS\text{-}MAX}$ (nm)	$\lambda_{PL\text{-}VIS\text{-}MAX}$ (nm)	Stokes Shift (nm)	PLQY[a]
A1 only	358	432	74	0.84%
1:1	357.5	432	75.5	0.75%
1:5	357	432	75	0.67%

[a] Quinine solution: 10^{-5} M in 0.05 M $H_2SO_{4(aq)}$ solution

Sample solvent: acetone

$\Phi_x = \Phi_{std}(I_x/I_{std})(A_{std}/A_x)(n_x/n_{std})^2$, $n_x = n_{acetone} = 1.355$, $n_{std} = 1.333$

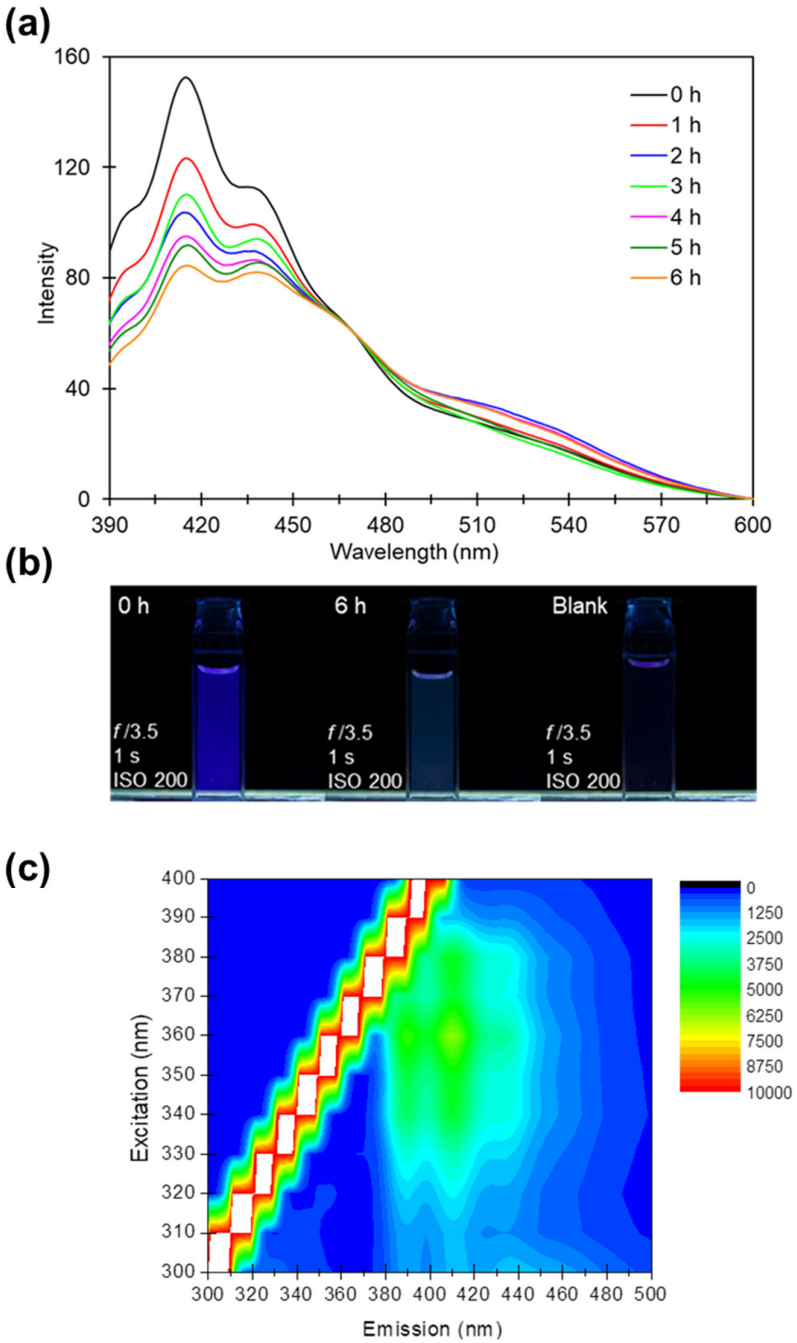

Fig. S34. (a) Photoluminescence spectra of **PR1** in CH_2Cl_2 (1×10^{-4} M) upon excitation at 360 nm after different irradiation times. (b) Photographs of **PR1** solutions in CH_2Cl_2 after various irradiation durations, with blank solvent shown for comparison (left to right). (c) Color-filled contour plot of fluorescence emission spectra upon excitation from 310 to 400 nm at 10 nm intervals.

S6. Photothermal Conversion

The photothermal conversion efficiency (η) was estimated from the time-dependent temperature profiles (**Fig. 6**) and corresponding linear fits in the temperature decay region (**Fig. S35**), using the following equation: $\eta = [hs(\Delta T_{\text{Sample-PBMA}} - \Delta T_{\text{PBMA}})]/I(1\text{-}10^{-A})$ with the relationship: $\tau = mc/hs$, where h is the heat transfer coefficient, s is the surface area of the sample, $\Delta T_{\text{Sample-PBMA}}$ and T_{PBMA} are the steady-state temperature change of the sample and the PBMA blank, respectively. I represents the laser power, A is the absorbance at the laser wavelength, τ is the time constant obtained from the linear fitting of the cooling curve, m is the mass of the sample, and c is the specific heat capacity of PBMA (1669 J kg^{-1} K^{-1}). The estimated values are summarized in **Table 1**.

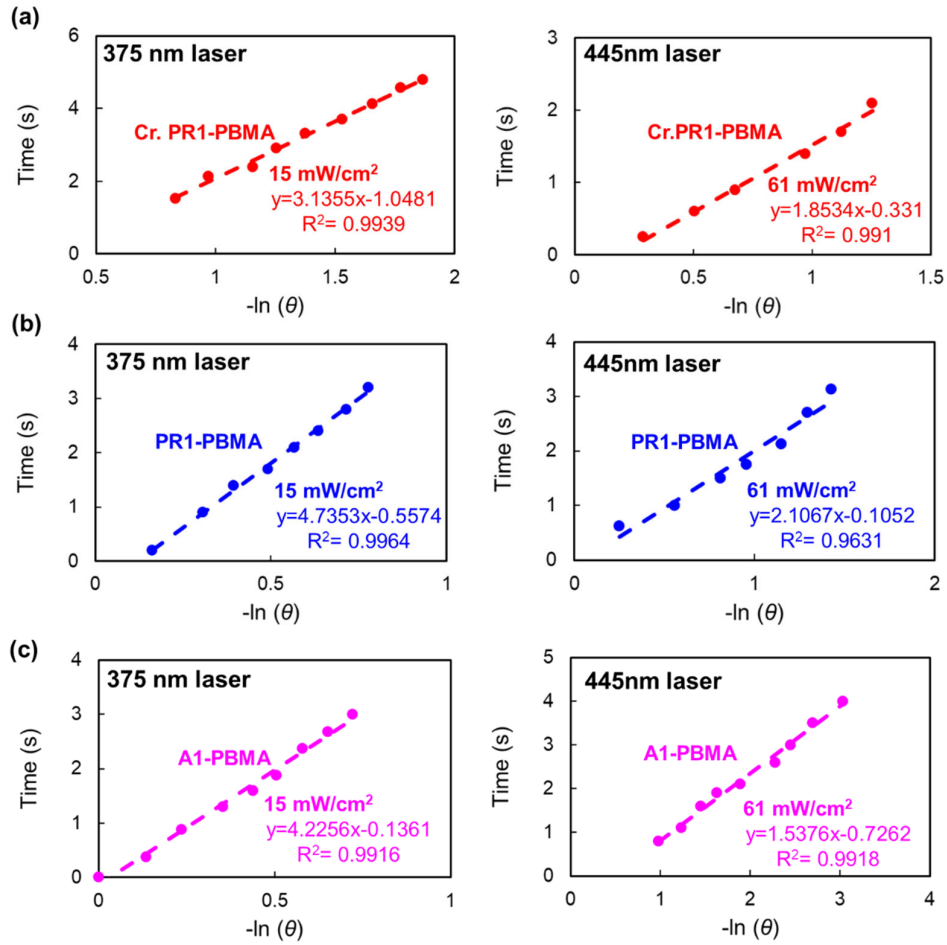

Fig. S35. Plots of the negative natural logarithm of the temperature driving force during the cooling stage for (a) **Cr.PR1-PBMA**, (b) **PR1-PBMA**, and (c) **A1-PBMA**.

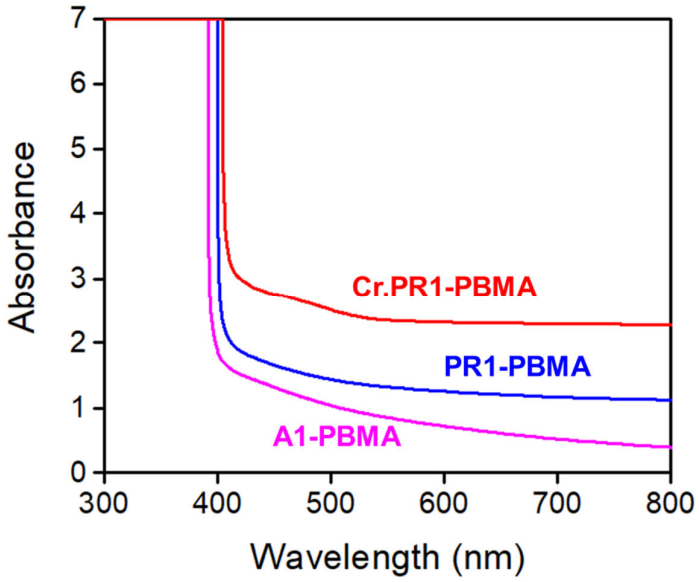

Fig. S36. UV-Vis spectra of PBMA films.

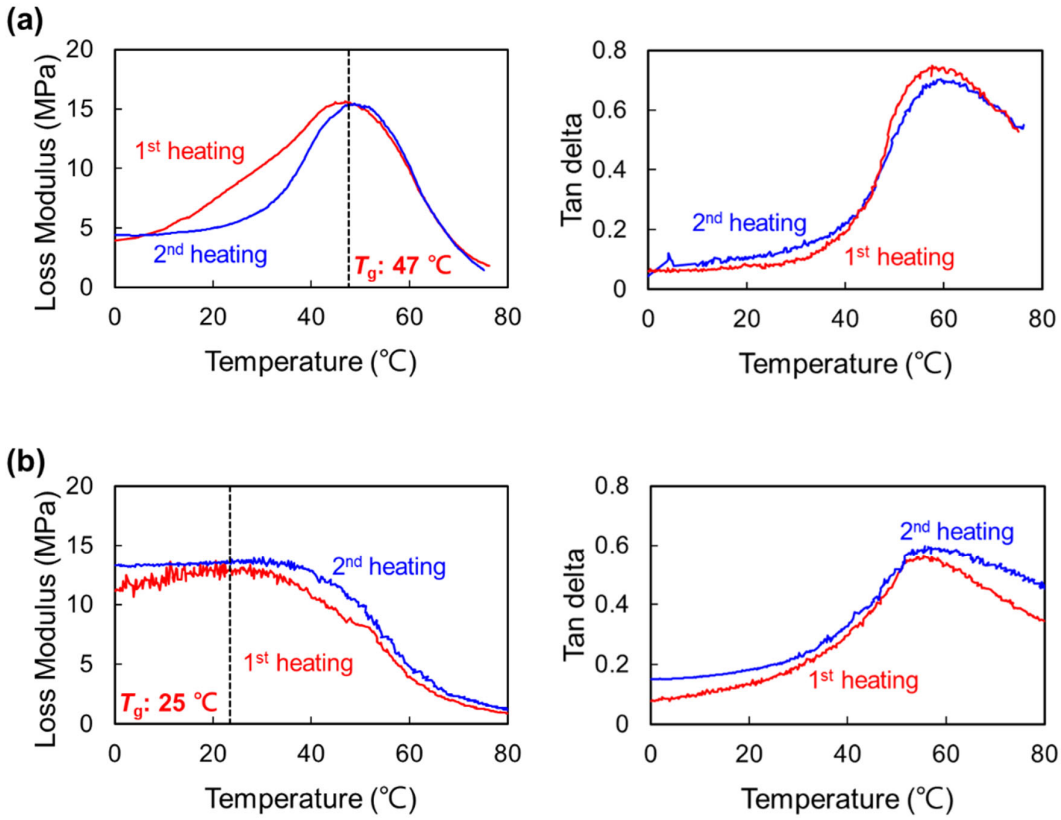

Fig. S37. DMA profiles of (a) **PR1-PBMA** and (b) **A1-PBMA**, showing loss modulus (right) and tan δ (left).

S7. Photoinduced Deformation and Mechanical Output

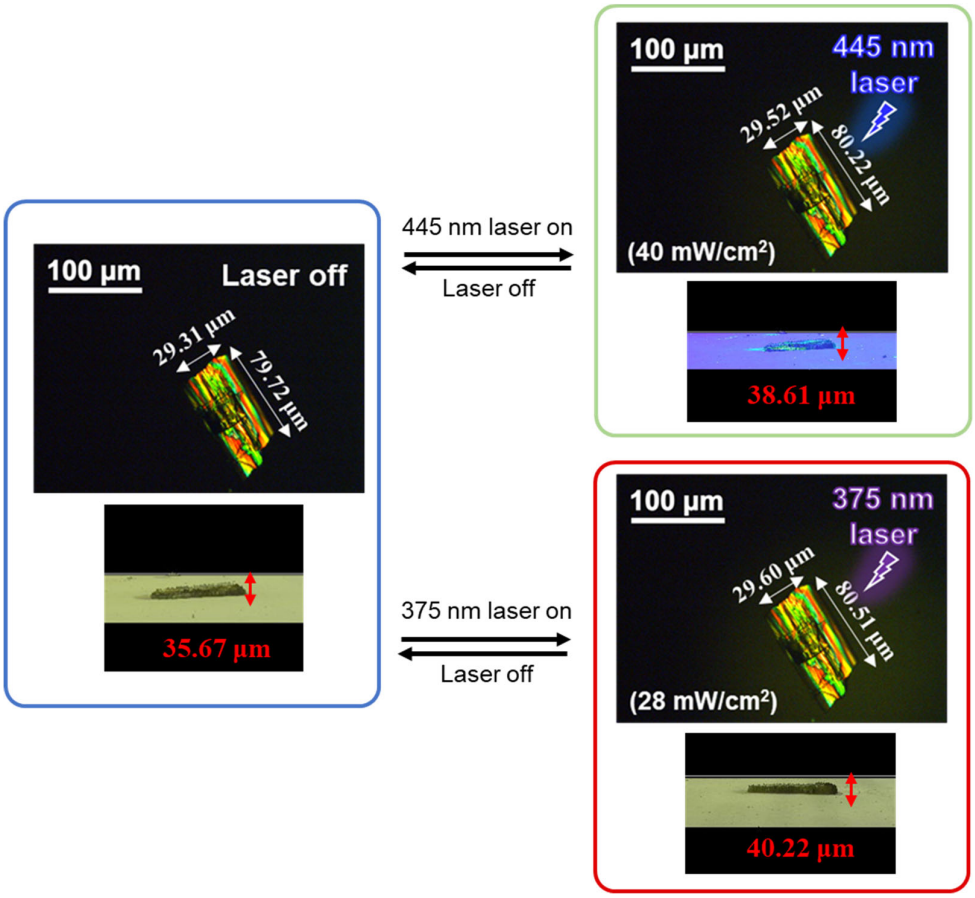

Fig. S38. Deformation behavior of **PR1** under 445 nm laser irradiation (40 mW cm^{-2}) and 375 nm laser irradiation (28 mW cm^{-2}).

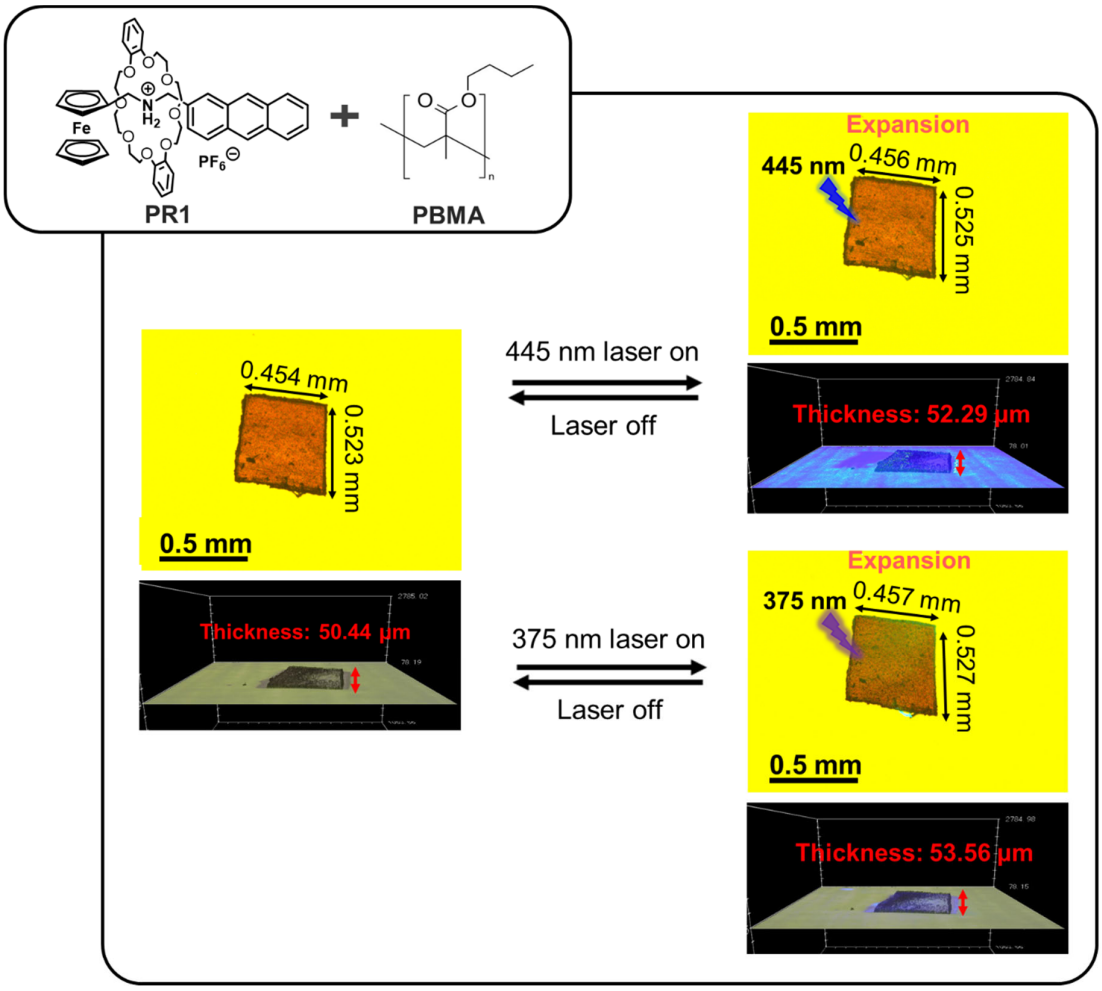

Fig. S39. Deformation behavior of **PR1-PBMA** under 445 nm laser irradiation (40 mW cm^{-2}) and 375 nm laser irradiation (28 mW cm^{-2}).

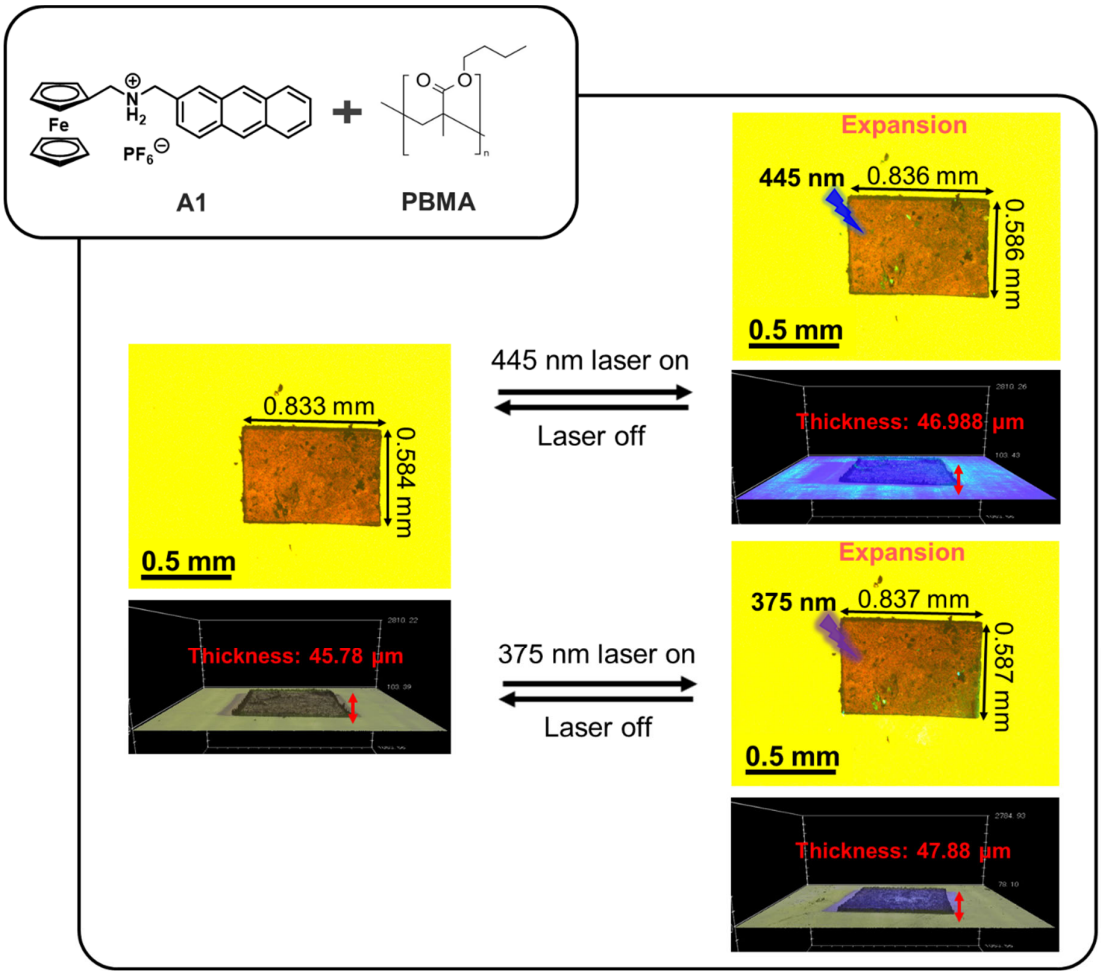

Fig. S40. Deformation behavior of **A1-PBMA** under 445 nm laser irradiation (40 mW cm^{-2}) and 375 nm laser irradiation (28 mW cm^{-2}).

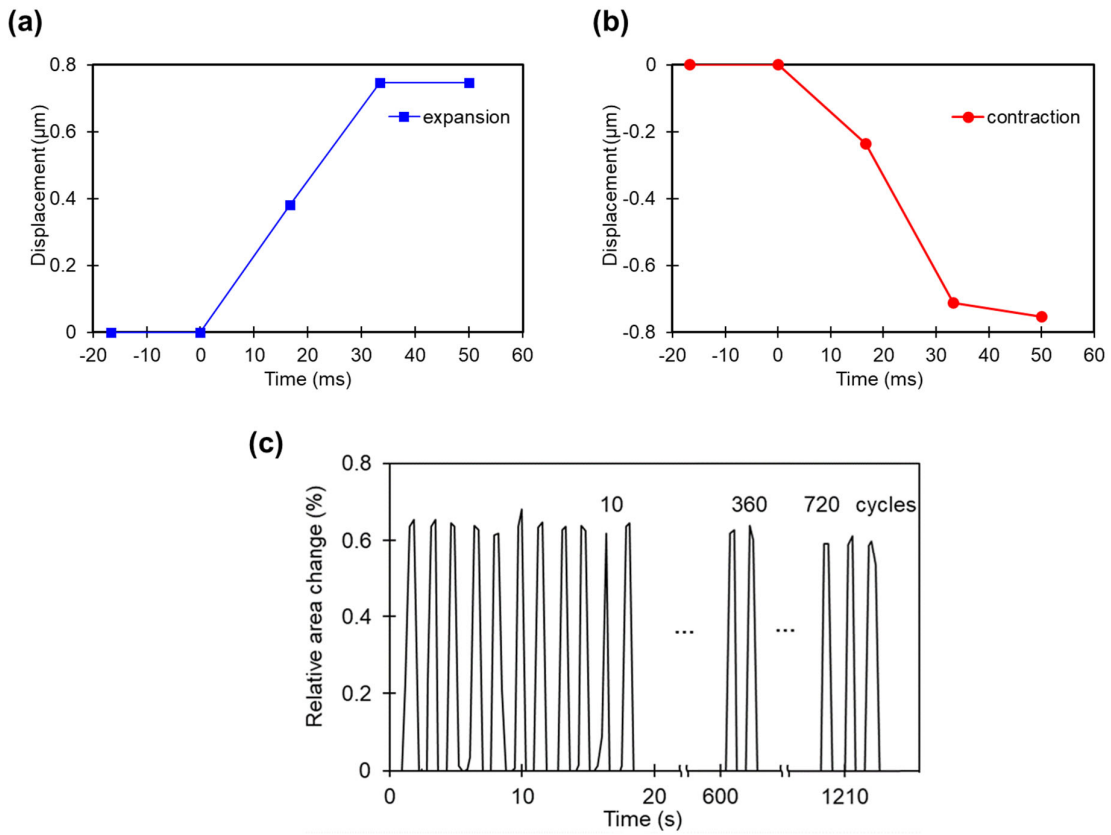

Fig. S41. Time dependence of the displacement of **PR1** induced by 445-nm laser (50 mW cm^{-2}). (a) Crystal expansion with laser on, (b) contraction with laser off, and (c) repeated relative area change.

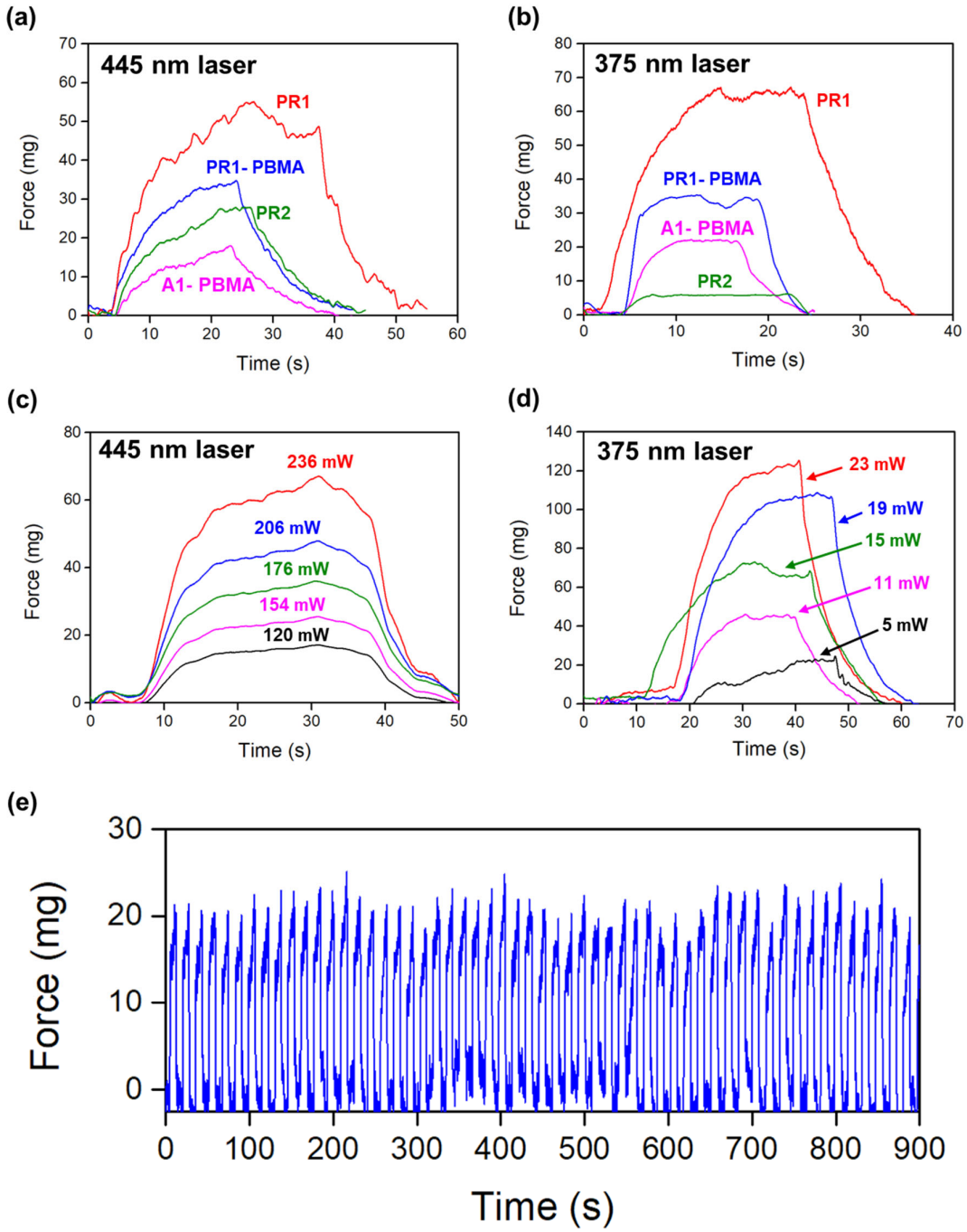

Fig. S42. Time-dependent force measurements under laser irradiation: (a) force response of different materials under 445 nm laser (220 mW cm^{-2}), (b) under 375 nm laser (15 mW cm^{-2}), (c) force response of a **PR1** crystal under 445 nm laser, (d) under 375 nm laser, and (e) force response of **PR1** under 445 nm laser at a power of 120 mW cm^{-2} with an on/off cycle of 8s/8s.

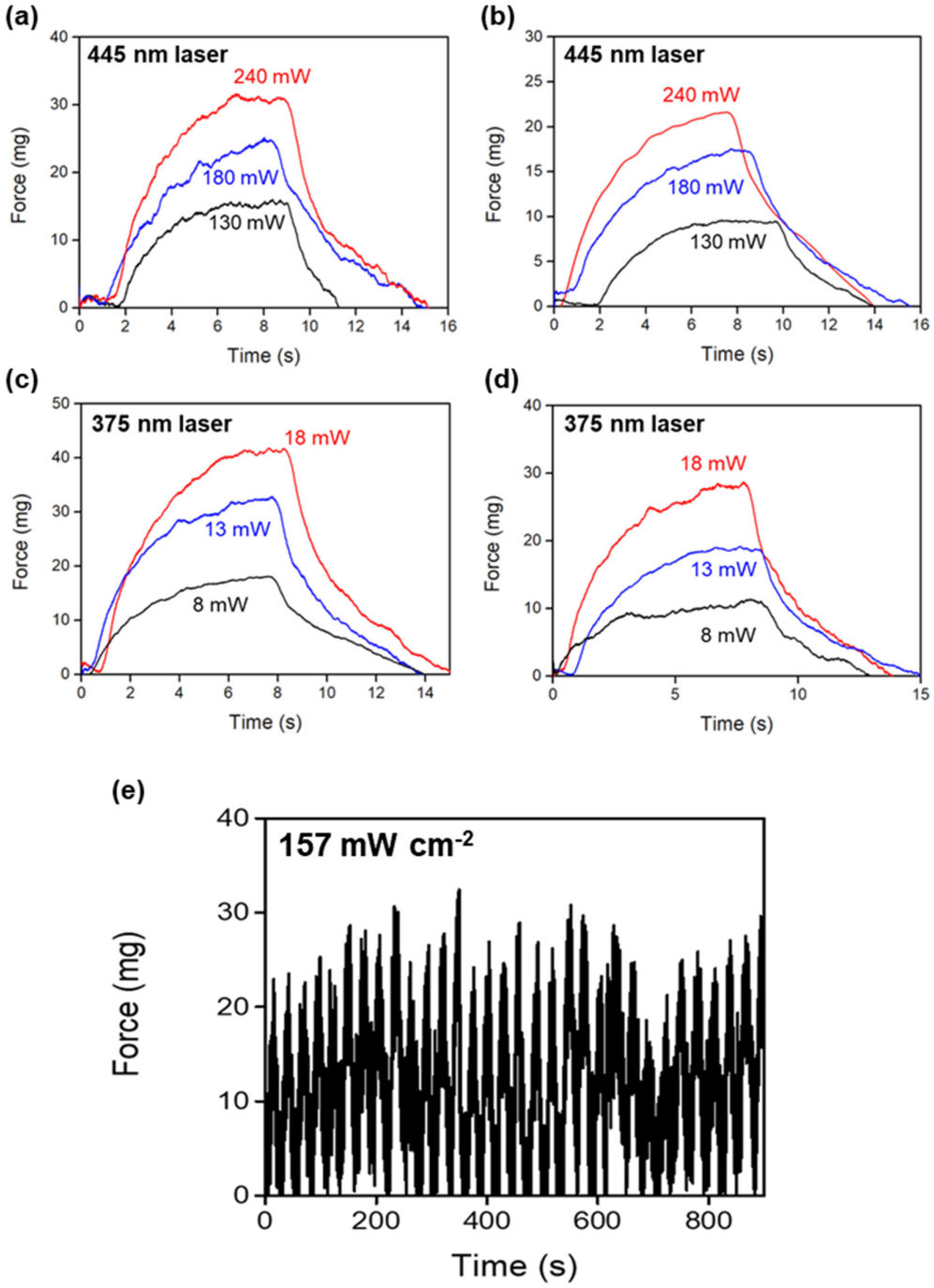

Fig. S43. Time-dependent force measurements under laser irradiation: (a) **PR1-PBMA** and (b) **A1-PBMA** under 445 nm laser, (c) **PR1-PBMA** and (d) **A1-PBMA** under 375 nm laser. (e) Force response of **PR1-PBMA** under 445 nm laser (157 mW cm^{-2}) with an on/off cycle of 15s/15s.